Structural basis of closed groove scrambling by a TMEM16 protein

Zhang Feng[1], Omar E. Alvarenga[2], Alessio Accardi[1,3,4#]

1 Department of Anesthesiology, Weill Cornell Medical College; 2 Physiology, Biophysics and Systems Biology Graduate Program, Weill Cornell Medical College; 3 Department of Physiology and Biophysics, Weill Cornell Medical College; 4 Department of Biochemistry, Weill Cornell Medical College

correspondence to: Alessio Accardi, ala2022@med.cornell.edu

Abstract

Activation of Ca^{2+}-dependent TMEM16 scramblases induces the externalization of phosphatidylserine, a key molecule in multiple signaling processes. Current models suggest that the TMEM16s scramble lipids by deforming the membrane near a hydrophilic groove, and that Ca^{2+} dependence arises from the different association of lipids with an open or closed groove. However, the molecular rearrangements involved in groove opening and of how lipids reorganize outside the closed groove remain unknown. Using cryogenic electron microscopy, we directly visualize how lipids associate at the closed groove of Ca^{2+}-bound nhTMEM16 in nanodiscs. Functional experiments pinpoint the lipid-protein interaction sites critical for closed groove scrambling. Structural and functional analyses suggest groove opening entails the sequential appearance of two π-helical turns in the groove-lining TM6 helix and identify critical rearrangements. Finally, we show that the choice of scaffold protein and lipids affects the conformations of nhTMEM16 and their distribution, highlighting a key role of these factors in cryoEM structure determination.

38 **Introduction**

39 Activation of phospholipid scramblases disrupts the plasma membrane asymmetry, and results in
40 the exposure of the negatively charged lipids phosphatidylserine (PS), an important signaling
41 molecule. Thus, lipid scrambling plays a key role in a variety of physiological processes, ranging
42 from recognition of apoptotic cells by macrophages and blood coagulation, to viral entry,
43 membrane fusion and repair [1-3]. To date, three families of integral membrane proteins have been
44 identified as lipid scramblases, the Ca^{2+}-activated TMEM16s [4-7] , the caspase-dependent XKRs [8],
45 and the ATG9 proteins involved in autophagosome formation [9-11]. Additionally, several other
46 proteins and single-helix membrane spanning peptides have been reported to mediate lipid
47 scrambling [12-16]. These scramblases share broadly conserved functional characteristics, such as
48 mediating rapid and poorly selective lipid transport [1-3,6,7], while displaying a remarkable structural
49 diversity, as each family adopts a different fold [7,9-11,17-22]. Thus, it is not known whether these
50 diverse scramblases function according to a conserved mechanism.

51 The currently accepted paradigm for lipid scrambling, the so-called credit-card mechanism,
52 is that scramblases provide a hydrophilic pathway that shields the polar lipid headgroups as they
53 traverse the bilayer, while the acyl chains remain embedded in the hydrocarbon core of the
54 membrane [7,23]. In several dimeric TMEM16 scramblases, Ca^{2+} binding favors opening of a
55 transmembrane hydrophilic groove which has been proposed to serve as the translocation pathway
56 for lipid headgroups [7,24-28]. The lipid groove is formed by TM3-7 helices of each TMEM16
57 protomer, and its interior is lined by hydrophilic residues [7] (Fig. 1a-c and f-h). In the apo
58 conformation, the TM4 and TM6 form an extensive interface that seals the groove interior from
59 the hydrocarbon core of the membrane (Fig. 1a, f), resulting in a closed groove. The Ca^{2+} binding
60 sites are located between TM6-8 and their formation is enabled by a rearrangement of the
61 intracellular portion of TM6 (Fig. 1b, g). Groove opening follows Ca^{2+} binding and entails a
62 movement of the TM3 and TM4 helices away from TM6 [17,18,21] (Fig. 1c, h). However, Ca^{2+} binding
63 does not promote groove opening in all TMEM16 scramblases as the mammalian TMEM16F
64 exclusively adopts a Ca^{2+}-bound closed groove conformation, even in conditions of maximal
65 activity [19,22,29], leading to the proposal that the closed groove is also a scrambling competent state
66 [19,30,31]. Gain-of-function mTMEM16F mutants adopt conformations where the groove remains
67 closed, but with a rearranged TM4-6 interface [29], raising the possibility that different closed-groove
68 conformations might be scrambling competent. Thus, how Ca^{2+} binding to the TM6-lined sites

69 induces the rearrangement of TM3 and TM4 to induce groove opening in some but not all
70 TMEM16s is not known.

71 Cryogenic electron microscopy (cryoEM) imaging of TMEM16 scramblases in nanodiscs
72 showed these proteins induce a pronounced thinning of the membrane near the groove region, a
73 distortion that is more pronounced when the groove opens [17,21,30]. However, resolution of these
74 structures was insufficient to visualize how individual lipids interact with the groove in the open
75 and closed conformations. Recently, high-resolution structures of the Ca^{2+}-bound fungal
76 afTMEM16 with an open groove revealed that lipids adopt distorted poses with their headgroups
77 positioned outside the pathway, providing the bases for membrane thinning near the open groove
78 [30]. Further, functional experiments suggested that specific interactions between groove-lining
79 residues and lipid headgroups are not required for open groove scrambling [30]. Together, these
80 observations led to the proposal that scrambling at an open groove is enabled by membrane
81 thinning [30], rather than occurring via a credit card mechanism. Because membrane thinning is also
82 observed in conditions when the groove is closed, it was proposed that afTMEM16 [30] and
83 TMEM16F [19,30,31] could scramble lipids outside a fully closed groove, or one with a rearranged
84 TM4-TM6 interface [29]. This proposal could also account for the basal activity of many TMEM16
85 scramblases in the absence of Ca^{2+} when the groove is closed [5,7,18]. However, direct structural
86 information on how lipids arrange near a closed groove is lacking, and it is not known whether or
87 how their arrangement plays a role in closed groove scrambling.

88 One important factor to consider when interpreting cryoEM imaging experiments is the
89 potential role of the environment in determining the conformation and state distribution of proteins.
90 For example, the Ca^{2+}-bound human TMEM16K scramblase crystalizes with an open groove but
91 has a closed groove in single particle cryoEM imaging conditions [18], and the fungal nhTMEM16
92 adopts conformations with an open, closed, and intermediate-closed groove with roughly equal
93 probability when reconstituted in MSP2N2 nanodiscs but is only in an open groove state when
94 imaged in detergent micelles with cryoEM and x-ray crystallography [7,21]. In contrast, other
95 homologues, such as murine TMEM16F and fungal afTMEM16 are less sensitive to the
96 environment, as they exclusively adopt a single conformation in detergent and in nanodisc
97 environments [17,19,22,30]. Thus, the extent to which choices of detergent, lipid and/or nanodisc
98 scaffold protein influence the conformation of TMEM16 scramblases is poorly understood.

99 Here, we used cryoEM to image the fungal nhTMEM16 scramblase in lipid nanodiscs
100 formed from different scaffold proteins and found this to affect both the conformations adopted by
101 nhTMEM16 and their distribution. In the smaller MSP1E3 nanodiscs the scramblase preferentially
102 adopts a closed conformation, whereas in the larger MSP2N2 nanodiscs nhTMEM16
103 predominantly adopts open and intermediate-open conformations. The 2.64 Å resolution structure
104 of Ca^{2+}-bound closed nhTMEM16 reveals how lipids arrange near the groove, thus showing how
105 the scramblase thins the membrane outside a closed groove. Mutating residues that coordinate
106 outer leaflet lipids near the closed groove impairs scrambling only in the absence of Ca^{2+},
107 suggesting these interactions play a specific role in closed-groove scrambling. Structural analysis
108 of the transition of nhTMEM16 from closed to open state suggests that the E313-R432 salt bridge
109 could be involved in groove opening. Disruption of this interaction by the R432A mutation trapped
110 nhTMEM16 in a closed-groove conformation, suggesting the salt bridge is critical for groove
111 opening. In sum, our work provides insights into how lipids are scrambled outside a closed groove,
112 how the groove opens, and how these processes are regulated by the lipid environment.
113
114 **Results**
115 **The conformational landscape of nhTMEM16 depends on the environment**
116 To understand how the environment affects the conformational landscape of TMEM16
117 scramblases, we focused on the fungal nhTMEM16 as this homologue can adopt multiple
118 conformations in different reconstitution systems [7,21]. We imaged the scramblase in the absence
119 and presence of Ca^{2+} and in nanodiscs formed from a 7:3 mixture of 1,2-Dioleoyl-sn-glycero-3-
120 phosphocholine (DOPC) and 1,2-Dioleoyl-sn-glycero-3-phosphatidylglycerol (DOPG) lipids. We
121 used the MSP1E3 and/or MSP2N2 scaffold proteins that differ in their average diameter by ~3 nm
122 [32,33]. In 0 Ca^{2+} and in MSP1E3 nanodiscs, we obtained a single class of particles, which yielded a
123 map with average resolution of 2.93 Å corresponding to a conformation with a closed hydrophilic
124 groove and no density in the Ca^{2+} binding sites (Fig. 1a, f and Extended Data Fig. 1). While this is
125 similar to what was reported for nhTMEM16 in nanodiscs formed with the larger MSP2N2 and
126 POPC:POPG lipids, there are differences in the Ca^{2+} sites and position of the cytosolic domains
127 (see below). In contrast, the conformational distribution of nhTMEM16 changes drastically when
128 reconstituted in 0.5 mM Ca^{2+} in MSP1E3 or MSP2N2 nanodiscs. We found that in MSP2N2
129 nanodiscs the majority of the particles (~69.2%) adopt an open groove conformation, ~17.3% are

130 in an intermediate-open state (see below), and no class with a closed groove could be detected (Fig.
131 1d-e, i-j and Extended Data Fig. 2). The remaining ~13.5% particles have poorly defined TM4
132 helices and could not be assigned (Extended Data Fig. 2). This is different from the findings in
133 MSP2N2 POPC/POPG nanodiscs [21], where the closed groove conformation was also significantly
134 populated. In the smaller MSP1E3 nanodiscs nhTMEM16 predominantly adopts a closed groove
135 conformation (~68.5% of particles) (Fig. 1b, g and Extended Data Fig. 3) and only a small fraction
136 is in an open groove conformation (~3.5% of particles) (Fig. 1c, h and Extended Data Fig. 3). In
137 the remaining ~28% of particles the density around the groove region was not well resolved,
138 suggestive of conformational heterogeneity. Classification of the symmetry-expanded and signal-
139 subtracted protomers from this subset shows that ~16% adopt a conformation with a closed groove,
140 ~15% are in an intermediate conformation and ~11% have an open groove (Extended Data Fig. 3
141 and 4). In the remaining ~58% protomers the density for TM4 is of insufficient quality for model
142 building but is consistent with the groove being in closed or intermediate conformations (Extended
143 Data Fig. 4). Mapping these protomers to the original dimeric particles allowed for a reconstruction
144 of a nhTMEM16 dimer with one open and one closed groove (Extended Data Fig. 3), consistent
145 with the idea that the protomers can gate autonomously [34,35]. In sum, these results show that the
146 open groove conformation of nhTMEM16 is favored >20-fold by reconstitution in the larger
147 MSP2N2 nanodiscs (Fig. 1k).

148 Next, we analyzed whether the choice of nanodisc scaffold protein and lipid composition
149 also affect the structures of the observed nhTMEM16 conformations. Unexpectedly, we identified
150 several structural differences. The Ca^{2+}-free map of nhTMEM16 determined in MSP1E3
151 DOPC/DOPG nanodiscs (PBD: 6QM4, EMD: 4589) [21] differs from the previously determined one
152 in MSP2N2 POPC/POPG nanodiscs as the Ca^{2+} binding sites are empty (Extended Data Fig. 5a,
153 d), TM6 is bent, and the cytosolic domains move away from each other by ~4 Å (Extended Data
154 Fig. 5a). This conformation, with a bent TM6, empty Ca^{2+} sites, and separated cytosolic domains,
155 resembles that of Ca^{2+}-free afTMEM16 [17,30]. Indeed, the conformation of nhTMEM16 in 6QM4 is
156 structurally more similar to its Ca^{2+}-bound closed state (Cα r.m.s.d of 0.67 Å, Extended Data Fig.
157 5b) than to our apo conformation (Cα r.m.s.d. 1.76 Å, Extended Data Fig. 5c). These
158 rearrangements are likely due to the presence of an unassigned density in the Ca^{2+} binding sites in
159 the EMD-4589 map (Extended Data Fig. 5e). The identity of the ligand causing the observed

160 rearrangements is unknown. This suggests that ligand binding to one of two sites is sufficient to
161 induce a rearrangement in the cytosolic domains and TM6.

162 The Ca^{2+}-bound open conformation determined in MSP1E3 DOPC/DOPG nanodisc is
163 nearly identical to the previously determined open structure of nhTMEM16 determined in the
164 larger MSP2N2 POPC/POPG discs (PDB: 6QM9) [21] (Cα r.m.s.d ~0.58 Å, Extended Data Fig. 5h).
165 The open conformation in MSP2N2 DOPC/DOPG nanodiscs has a slightly more opened groove
166 than that in POPC/POPG lipids because of a lateral displacement of the TM4 by ~1.5 Å (Cα r.m.s.d
167 ~1.24 Å, Extended Data Fig. 5i). The Ca^{2+} bound closed conformations in MSP1E3 DOPC/DOPG
168 (PDBID: 6QMB) and MSP2N2 POPC/POPG are nearly identical (Cα r.m.s.d ~0.50 Å). Finally,
169 the intermediate conformation seen in the MSP2N2 DOPC/DOPG nanodiscs differs from the
170 previously reported intermediate-closed one, as the TM4 is shifted further away from TM6 by ~2
171 Å and accompanied with a counterclockwise rotation of the extracellular portion of TM4, such
172 that there is minimal contact between TM4 and TM6 (Cα r.m.s.d ~1.35 Å; Fig. 1lm and Extended
173 Data Fig. 5j). This repositioning results in a conformation where the groove, while remaining
174 isolated from the hydrocarbon core of the membrane, forms a continuous transmembrane pore that
175 is wide enough to accommodate water molecules and permeant ions such as K^+ and Cl^- (Fig. 1n-
176 o). This is consistent with the reported channel activity of nhTMEM16 [36,37] [38]. Therefore, we refer
177 to this conformation as intermediate-open. Together, our results show that the scaffold protein and
178 lipid composition affect both the distribution and structures of the conformations adopted by
179 nhTMEM16.

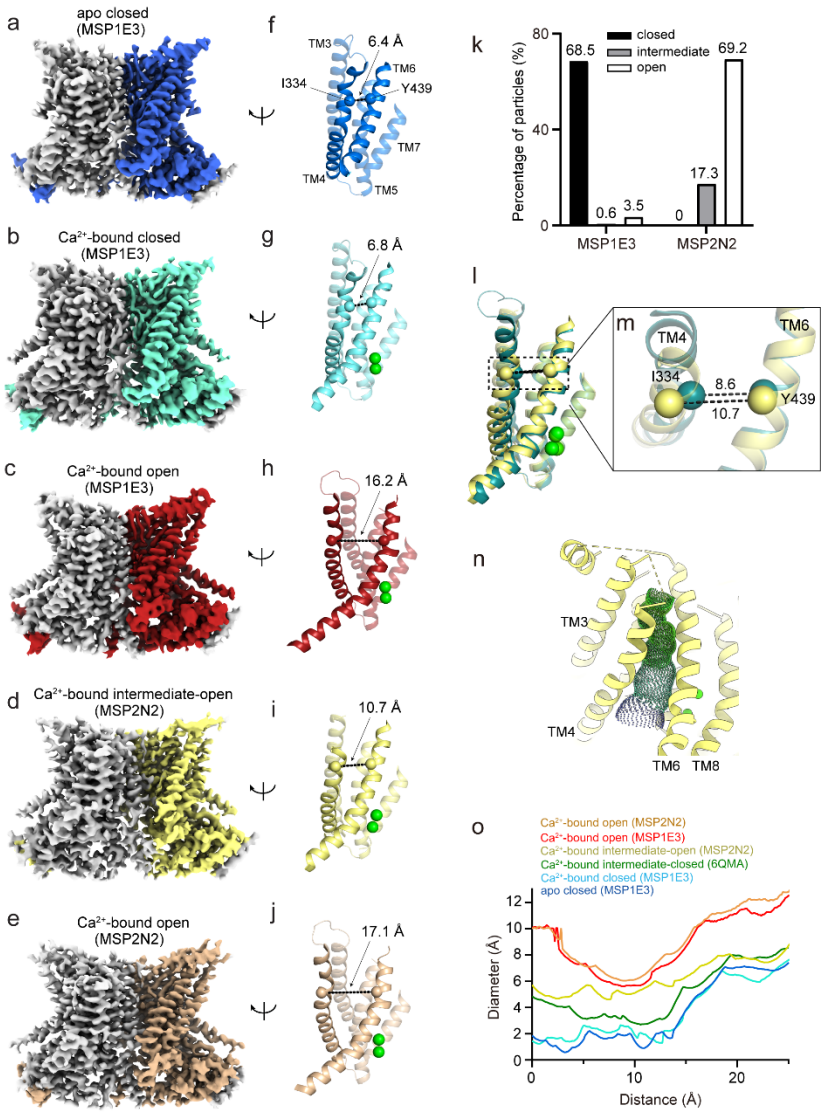

Figure 1. Cryo-EM structures of nhTMEM16 in the MSP1E3 and MSP2N2 nanodiscs. a-b, Cryo-EM maps of nhTMEM16 in nanodiscs formed from a 7:3 mix of DOPC:DOPG lipids and MSP1E3 (**a-c**) or MSP2N2 (**d-e**) scaffold proteins. (**a**) Ca^{2+}-free, closed groove, (**b**) Ca^{2+}-bound, closed groove, (**c**) Ca^{2+}-bound, open groove, (**d**) Ca^{2+}-bound, intermediate-open groove, and (**e**) Ca^{2+}-bound, open groove. In all dimers, one protomer is colored in gray and the other in blue (**a**), cyan (**b**), red (**c**), yellow (**d**), and sand (**e**). **f-j**, The groove in the different conformations is viewed from the plane of the membrane. Transmembrane helices are shown in cartoon representations and labelled. States are colored as in (**a-e**). Colored spheres correspond to the position of the Cα atoms of I334 on TM4 and Y439 on TM6 and their distance is indicated. Ca^{2+} ions are shown as green spheres. **k**, The percentage of particles with a closed (black bar), intermediate (gray bar), or open (white bar) groove conformation in the datasets of Ca^{2+}-bound nhTMEM16 in MSP1E3 or MSP2N2 nanodiscs. Here, intermediate does not distinguish between the intermediate-open and -closed conformations. **l-m**, Alignment of the groove helices in the intermediate-open (yellow) and previously reported intermediate-closed (PBD: 6QMA, dark green) states (**l**), the distance between the Cα atoms of I334 on TM4 and Y439 on TM6 increases by ~2 Å in the intermediate-open **(m)**. **n**, The accessibility of the permeation pathway of nhTMEM16 in the intermediate conformation is visualized using the program Hole [39]. **o**, The inner diameter of the permeation pathway of nhTMEM16 in MSP1E3 or MSP2N2 nanodiscs and in the published the diameter of a putative ion conduction pathway measured in different states with Hole including the Ca^{2+}-bound open state in MSP2N2 (orange), Ca^{2+}-bound open state in MSP1E3 (red), Ca^{2+}-bound intermediate-open state in MSP2N2 (yellow), Ca^{2+}-bound closed state in MSP1E3 (cyan), the previously reported intermediate-closed state in MSP2N2 (dark green) and Ca^{2+}-free closed in MSP1E3 (blue).

200

201 **Basis of membrane thinning at the closed groove of nhTMEM16**

202 The cryoEM map of Ca^{2+}-bound nhTMEM16 with a closed groove in MSP1E3 nanodiscs reached
203 an average resolution of 2.64 Å, allowing us to identify 36 well-defined non-protein densities, 18
204 on each protomer, that could be modeled as lipids (Fig. 2a-d and Extended Data Fig. 6). These
205 densities define nearly continuous inner (IL) and outer leaflets (OL) and thus outline the protein-
206 membrane interface (Fig. 2a-d and Extended Data Fig. 6a-e; Supplementary Video 1). In all cases
207 the headgroups of lipids are not well resolved, therefore lipids were only built up to the phosphate
208 atom. The 8 lipids near the dimer interface (D1-D8) define the inner and outer leaflets planes and
209 adopt similar positions to those seen in Ca^{2+}-bound open afTMEM16 [30] (Extended Data Fig. 6c-
210 e), consistent with the idea this region undergoes minimal rearrangements during groove opening.

211 The arrangement of the 10 lipids near the pathway (P1-P10) reveals the structural basis of
212 membrane thinning at a closed groove (Fig. 2d and Extended Data Fig. 6b). The outer leaflet P1-
213 P4 lipids become progressively more tilted as they approach the site of TM4-TM6 contact that
214 defines the groove closure (Fig. 2d) and their headgroups form extensive interactions with
215 aromatic and polar residues in TM1, TM4, TM6, and TM8 (Fig. 3c). Notably, the headgroups of
216 the P3 and P4 lipids adopt severely distorted poses (Fig. 2d) and interact with three aromatic
217 residues, Y327 and F330 on TM4 and Y439 on TM6 (Fig. 3b). The P5 and P6 lipids delimit the
218 inner leaflet across the wide intracellular vestibule of the pathway (Fig. 2d). The closest point of
219 approach of the two leaflets at the closed groove is defined by the phosphate atoms of P4 and P6
220 which are separated by only ~27 Å, so that the hydrocarbon core of the membrane is thinned by
221 ~30% (Fig. 2d). The Ca^{2+}-bound and Ca^{2+}-free closed conformations are nearly identical in this
222 region (Extended Data Fig. 7a-e), indicating that protein-lipid interactions are likely unchanged in
223 the two conformations. Thus, if the observed thinning is important for closed groove scrambling,
224 then we expect these residues to play similar roles in the Ca^{2+}-free and Ca^{2+}-bound closed states.

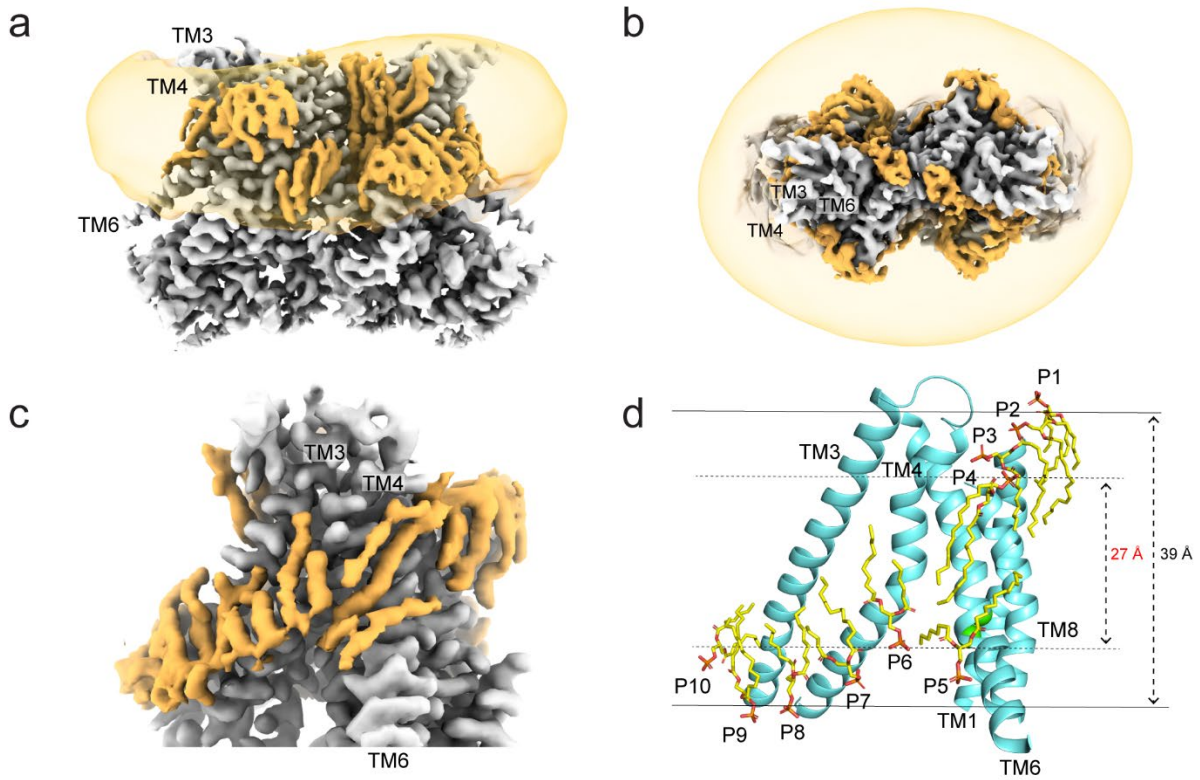

Figure 2. Arrangement of lipids at the closed groove of nhTMEM16. a-b, Segmented Cryo-EM map of nhTMEM16 in the Ca^{2+}-bound closed state (gray), in MSP1E3 nanodiscs and DOPC/DOPG lipids, and the associated lipids (orange) viewed from the membrane plane (**a**) and from the extracellular side (**b**). The map showing the density of the nanodisc membrane is low-pass filtered to 10 Å and shown in transparent orange. **c,** View of the lipids outside of the closed groove from the plane of the membrane. **d,** Stick representation of the ten pathway lipids colored in yellow (P1-P10). Dashed arrow indicates the distance between the phosphate atoms of the last lipid from the inner (P6) and outer (P4) leaflets (~27 Å) and the measured membrane thickness (~39 Å). Lipids were built up to the phosphate atom in the head. Ca^{2+} ions are displayed as green spheres.

Residues coordinating outer leaflet lipids are important in closed groove scrambling

To test this hypothesis, we designed three composite mutations aimed at disrupting coordination of the OL P1-P2-P3 (W210A/N435A/F438A/Y439A/W521A) and P3-P4 lipids (Y327A/F330A/Y439A) or of the IL P6-P10 lipids (M348A/G349A/M353A/K357A) (Fig. 3a-c) and tested their effects using a well-established in vitro assay to measure their effects on scrambling activity [5,40,41]. In the presence of 0.5 mM Ca^{2+}, when scrambling is primarily mediated by the open groove, the three constructs have WT-like rate constants (Fig. 3d-g, i). In contrast, in 0 Ca^{2+}, when the groove is closed, the two constructs disrupting interactions with OL lipids display an 8- and 6-fold reduction in scrambling activity ($p<10^{-7}$) (Fig. 3d-h). The scrambling rate constants of the mutant disrupting interactions with IL lipids are not statistically different from WT ($P>0.4$) (Fig. 3i). Thus, these mutants impair scrambling only in the absence of Ca^{2+}, when

the groove is closed, but have no effect in the presence of Ca^{2+}, when the groove can open, suggesting that the two processes are mediated by different conformations. Therefore, we hypothesize that nhTMEM16, like afTMEM16 [30] and mTMEM16F [19], can scramble lipids with a closed groove and that remodeling of the OL lipids play a critical role in this process.

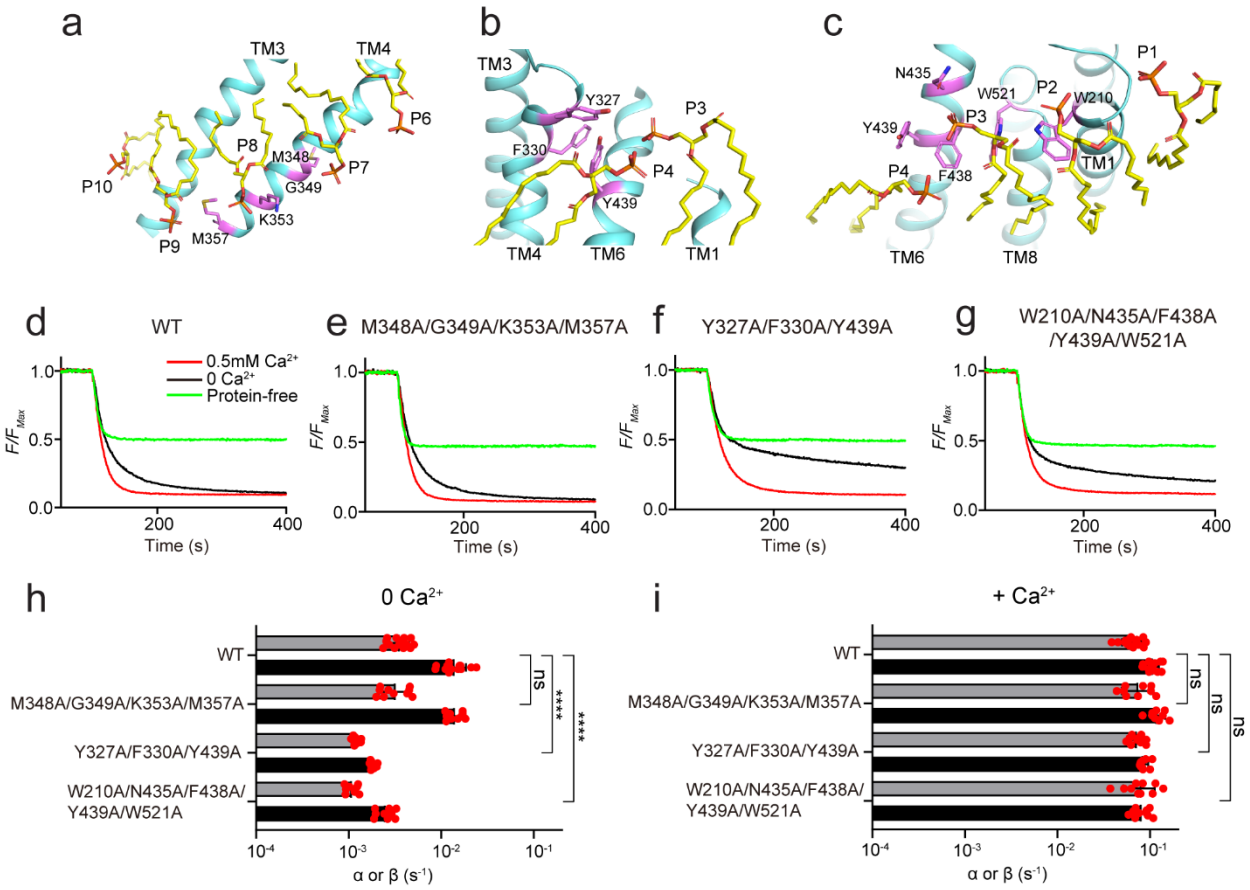

Figure 3. Identification of residues important for the closed groove scrambling. a-c, Residues coordinating the P7-P9 (**A**), P3-P4 (**B**) and P2-P4 lipids (**C**) in the Ca^{2+}-bound closed state. **d-h**, Representative traces of the dithionite induced fluorescence decay in the scrambling assay for protein free liposomes (green), or WT and the mutants in the presence (red) and absence (black) of Ca^{2+}. **h-i**, Forward (α) and reverse (β) scrambling rate constants of the mutants of nhTMEM16 aimed at disrupting the protein-lipid interactions (shown in **a-c**) measured in 0 (**h**) or 0.5 mM Ca^{2+} (**i**). Bars are averages for α (black) and β (gray) (N ⩾ 3), error bars are S. Dev., and red circles are values from individual repeats. The statistical significance of the effects of the mutants on the scrambling rate constants was evaluated with a two-sided Student's t-test with a Bonferroni correction. **** denotes $p<10^{-5}$ after Bonferroni correction.

Steps in groove opening of nhTMEM16

Our structures captured nhTMEM16 in several conformations, that likely reflect intermediates as the protein transitions from a Ca^{2+}-free closed, to Ca^{2+}-bound closed, intermediate, and open states (Fig. 4a-b). For simplicity, we consider only the conformations determined in MSP1E3 nanodiscs,

as they have the highest resolution. In the Ca^{2+}-free closed state the TM6 is in an α-helical configuration (Fig. 4a). Ca^{2+} binding induces a clockwise rotation of the intracellular portion of TM6 around A444, which results in the appearance of a π-helical turn that allows the E452 side chain to coordinate the bound Ca^{2+} ion in the upper and lower sites (Fig. 4a and Extended Data Fig. 7f, g). When the groove opens there is a counterclockwise rotation of the central portion of TM6 (between R432 and V447, Fig. 4b), which leads to the formation of a second π-helical turn (Fig. 4b). This disrupts the tight packing of TM4-TM6 in the closed groove and thus might facilitate opening (Fig. 4b). During these rearrangements the extracellular portion of TM6 does not move much, likely because the salt bridge between R432 on TM6 and E313 on TM3 provides a stabilizing interaction (Fig. 4a, b), suggesting it might play a role in the opening transition.

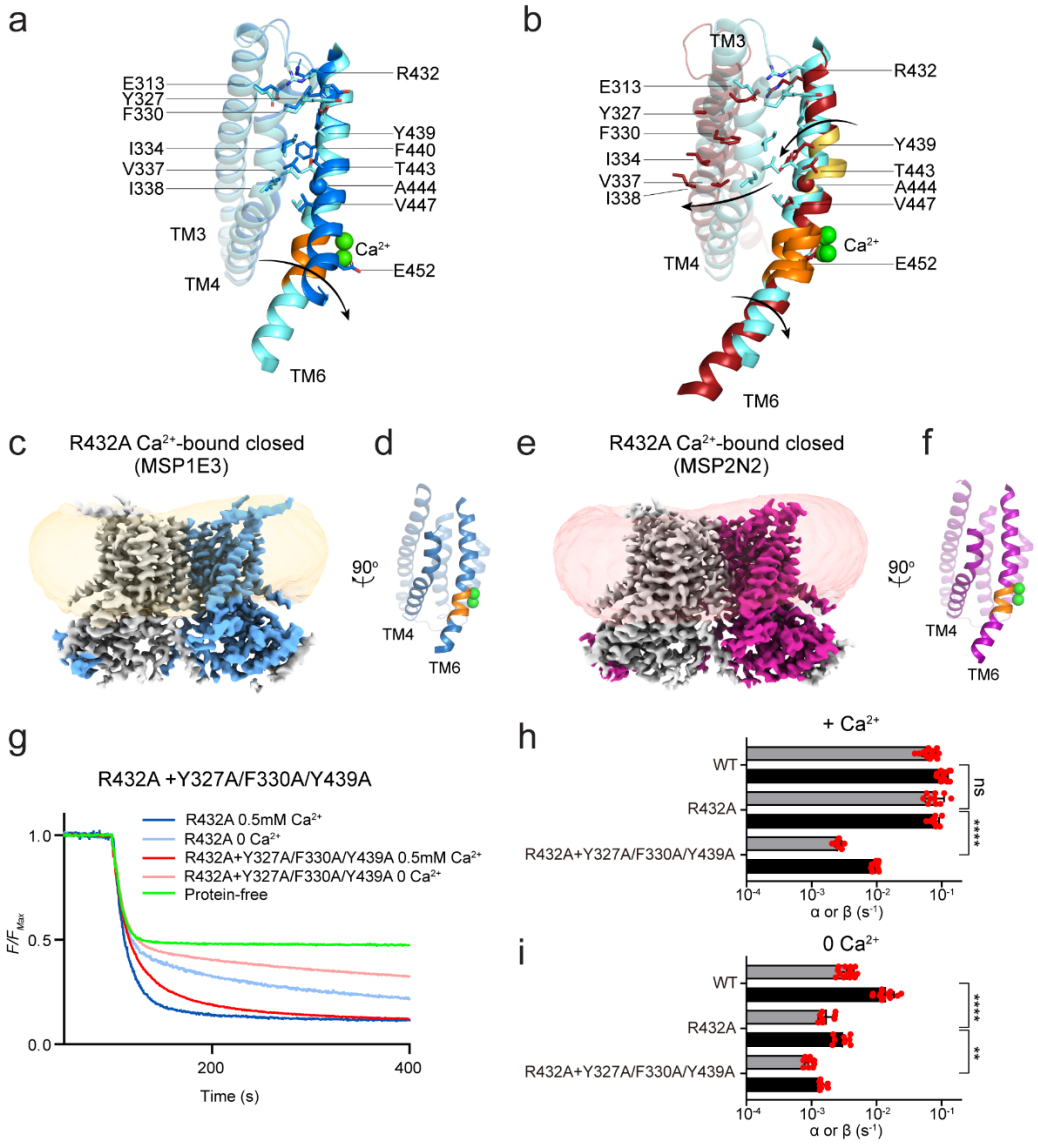

Figure 4. Role of the E313-R432 salt bridge in groove opening. **a-b**, Structural comparisons of the groove in apo (blue) vs Ca^{2+}-bound closed (cyan) (**a**) and Ca^{2+}-bound closed (cyan) vs open (red) states (**b**). Arrows denote rotations in the TM6. Sidechains of E313 and R432, and of the residues forming the TM4-TM6 interface are shown as sticks. The intra- and extra-cellular π-helical turns are colored in orange and gold, respectively. Ca^{2+} ions are displayed as green spheres. **c, d**, Cryo-EM maps of R423A nhTMEM16 in MSP1E3 (**c**) or MSP2N2 (**e**) nanodiscs. One protomer is colored in gray and the other in light blue (**c**) or magenta (**e**). The density of the nanodisc membrane is low pass filtered to 7 Å and shown in transparent orange (**c**) and red (**e**). **d, f**, Views of the groove from the plane of the membrane. TM4 and TM6 are shown in cartoon representation and labelled. Ca^{2+} ions are displayed as green spheres. **g**, Representative traces of the dithionite induced fluorescence decay in the scrambling assay for protein free liposomes (green), or R432A nhTMEM16 and the quadruple mutant R432A+Y327A/F330A/Y439A nhTMEM16 in the presence (dark blue and dark red) and absence (light blue and light red) of Ca^{2+}. **h-i**, Forward (α) and reverse (β) scrambling rate constants of the mutants measured in 0.5 mM (**h**) or 0 Ca^{2+} (**i**). Bars are averages for α (black) and β (gray) ($N \geqslant 3$), error bars are S. Dev., and red circles are values from individual repeats. The statistical significance of the effects of the mutants on the scrambling rate constants was evaluated with a two-sided Student's t-test with a Bonferroni correction. ** denotes $p<0.001$ and **** denotes $p< 10^{-5}$ after Bonferroni correction.

Disruption of the E313-R432 salt bridge favors a closed groove

To test this hypothesis, we used cryoEM to image R432A nhTMEM16 in MSP1E3 or MSP2N2 nanodiscs in the presence of 0.5 mM Ca^{2+} (Fig. 4c, e and Extended Data Fig. 8a-g). The maps have similar average resolutions of 3.59 Å and 3.64 Å and show that R432A nhTMEM16 adopts a single class with a fully closed groove (Fig. 4d, f). Despite multiple rounds of iterative 3D classifications on dimers and protomers using different classification parameters and software (Extended Data Fig. 8e), no classes displaying an open groove could be identified. The models for Ca^{2+}-bound R432A are nearly identical to that of WT Ca^{2+}-bound closed nhTMEM16 in MSP1E3 nanodiscs (Fig. 2d and Extended Data Fig. 8h-j), with Cα r.m.s.d. of ~0.93 and ~0.98 Å. Consistently, the R432A map displays strong density in both Ca^{2+} binding sites (Extended Data Fig. 8k, l) and only the intracellular π-helical turn is present on TM6 (Fig. 4d, f). The only difference from the WT structure is that the density corresponding to the extracellular portion of the TM4 helix is weakened (Fig. 4d, f and Extended Data Fig. 8m, n), suggesting this region becomes dynamic in the mutant. Thus, disruption of the TM6-TM3 salt bridge favors a closed groove conformation.

Next, we determined how the R432A mutation affects scrambling activity in DOPC/DOPG liposomes and found it retains WT-like activity in the presence of Ca^{2+} and a ~4-fold reduction in 0 Ca^{2+} ($p<10^{-5}$) (Fig. 4g-i). As the only visible conformation of Ca^{2+}-bound R432A nhTMEM16 in MSP1E3 and MSP2N2 nanodiscs is with a closed groove, we hypothesize its activity in the presence of Ca^{2+} reflects closed-groove scrambling. We tested this hypothesis by combining the R432A mutant with the triple Y327A/F330A/Y439A mutant which only impairs scrambling in 0 Ca^{2+} (Fig. 3d), when the groove is closed. We expected that if Ca^{2+} bound R432A mediates closed groove scrambling, then the quadruple mutant should display reduced activity in the presence of

314 Ca^{2+}, while neither of the original mutants did. In contrast, if scrambling by Ca^{2+}-bound R432A
315 occurs via an open groove mechanism, we would expect the quadruple mutant to have WT-like
316 activity. Results meet expectations: the R432A+Y327A/F330A/Y439A mutant displays an ~8-
317 fold reduction in scrambling activity in 0.5 mM Ca^{2+} ($p<10^{-5}$) (Fig. 4g-h), very similar to the effect
318 of the triple Y327A/F330A/Y439A in 0 Ca^{2+} (Fig. 3d). In the absence of Ca^{2+} the quadruple mutant
319 reduces scrambling activity ~9-fold (Fig. 4g, i). Together, these results suggest that the R432A
320 mutation favors a closed groove conformation by causing a decrease in Ca^{2+} potency and that
321 nhTMEM16 mediates Ca^{2+}-dependent closed-groove scrambling. However, we cannot rule out the
322 possibility that the chemical step in the dithionite assay limits our ability to accurately resolve the
323 effects of the mutants in the presence of Ca^{2+}. Similarly, it is possible that the open probability of
324 the Ca^{2+} bound R432A groove is too low to be detected in cryoEM imaging experiments but
325 sufficient to account for the observed activity in liposomes. Finally, we note that the R432A
326 mutation might also slightly perturb the conformation of the closed groove as it mildly impairs
327 scrambling in 0 Ca^{2+} (Fig. 4i).
328

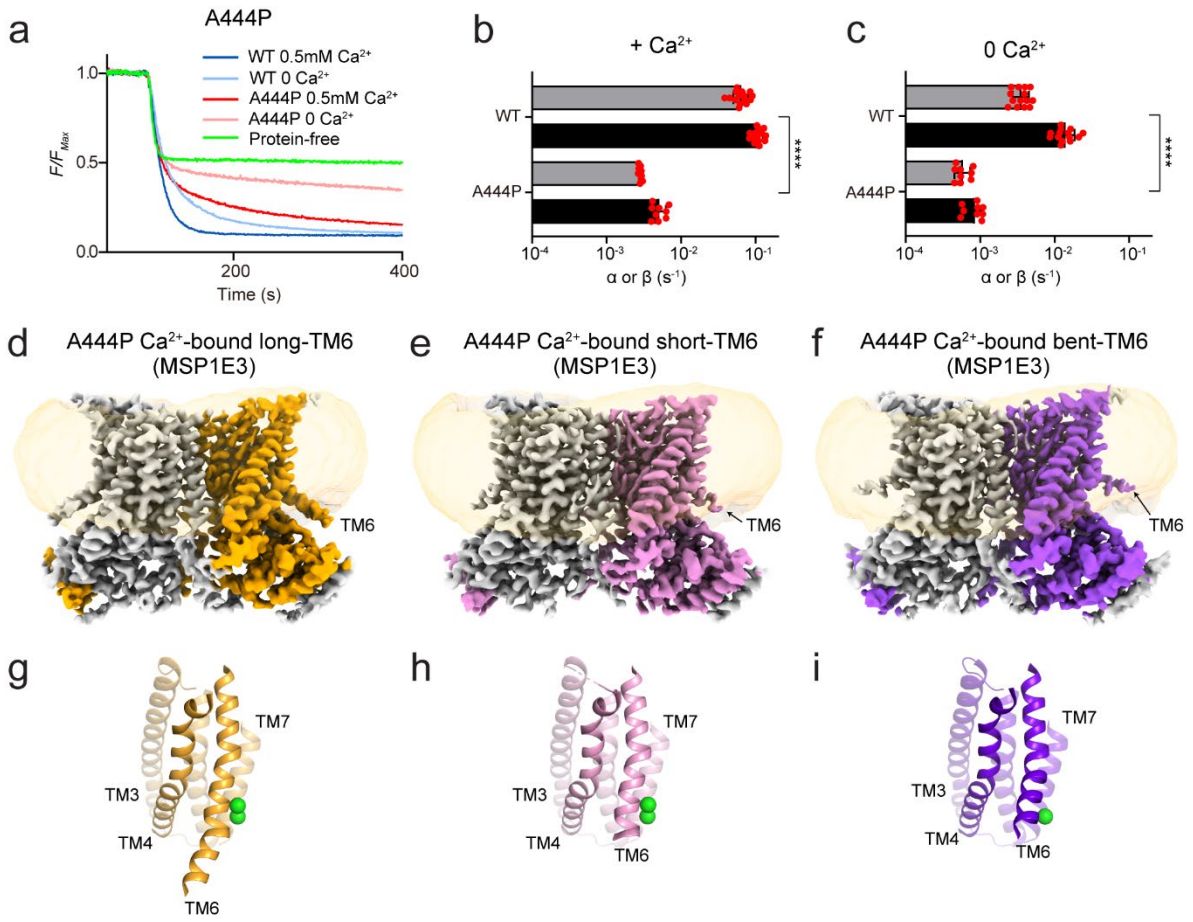

Figure 5. Disruption of TM6 straightening impairs lipid scrambling. a, Representative traces of the dithionite induced fluorescence decay in the scrambling assay in protein-free liposomes (green) or proteoliposomes reconstituted with WT and A444P nhTMEM16 in the presence (dark blue and dark red) and absence (light blue and light red) of Ca^{2+}. **b-c**, Forward (α) and reverse (β) scrambling rate constants of the mutants measured in 0.5 mM (**b**) or 0 Ca^{2+} (**c**). Bars are averages for α (black) and β (gray) (N ⩾ 3), error bars are S. Dev., and red circles are values from individual repeats. The statistical significance of the effects of the mutants on the scrambling rate constants was evaluated with a two-sided Student's t-test with a Bonferroni correction. **** denotes $p<10^{-5}$ after Bonferroni correction. **d-f**, Cryo-EM maps of A444P nhTMEM16 in MSP1E3 nanodiscs in the long TM6 state (**d**), short TM6 state (**e**) and bent TM6 state (**f**). One protomer is colored in gray and the other in orange (**d**), pink (**e**), and purple (**f**). The density of the nanodisc membrane is low pass filtered to 7 Å and shown in transparent orange. **g-i**, The groove in the long TM6 (**g**), short TM6 (**h**) and bent TM6 (**i**) states is viewed from the plane of the membrane. Transmembrane helices are labelled and Ca^{2+} ions are displayed as green spheres.

Straightening of TM6 is important for closed-groove scrambling

One key assumption of the closed groove scrambling model is that the structural differences between the apo-closed and Ca^{2+}-bound closed conformations underlie the Ca^{2+} dependence of some TMEM16 scramblases. In our structures the major difference occurring on Ca^{2+} binding is the straightening of the intracellular portion of the TM6 helix around A444 and the formation of

349 the intracellular π-helical turn (Fig. 4a and Extended Data Fig. 7f, g). To investigate whether this
350 rearrangement modulates closed groove scrambling we introduced a helix-bending proline at
351 position A444. The A444P mutant displays severely impaired scrambling activity in DOPC/DOPG
352 liposomes, with a >20-fold reduction in 0.5 mM Ca^{2+} and ~17-fold reduction in 0 Ca^{2+} ($p<10^{-8}$)
353 (Fig. 5a-c). Cryo-EM imaging of A444P nhTMEM16 in MSP1E3 DOPC/DOPG nanodiscs in 0.5
354 mM Ca^{2+} (Fig. 5d-I and Extended Data Fig. 9a-i) shows the mutant exclusively adopts
355 conformations with a closed groove (Cα r.m.s.d. <0.4 Å to WT Ca^{2+}-bound nhTMEM16 in all
356 cases). Extensive classification results in four dimer classes: three are symmetrical and differ only
357 in the occupancy of the Ca^{2+} binding sites and in the conformation of the intracellular portion of
358 TM6 below 444P (Fig. 5d, f and Extended Data Fig. 9j-l), and we refer to them as 'long TM6'
359 (~1.3% of particles), 'short TM6' (~45% of particles), and 'bent TM6' (~4.5% of particles). The
360 fourth class is asymmetric, with one protomer in the long TM6 and one in the short TM6
361 conformations (21.8% of particles) (Extended Data Fig. 9a-i). In the remaining ~27% of particles
362 the density of the TM6 helices is not well defined, and therefore could not be assigned to any of
363 the classes. Whereas in the long TM6 map the density for both Ca^{2+} binding sites is similar (Fig.
364 5d, g and Extended Data Fig. 9j), in the short TM6 map the density in the upper Ca^{2+} binding site
365 is weaker than that in the bottom site (Fig. 5e, h and Extended Data Fig. 9k). In the bent TM6
366 conformation the E452 side chain on TM6 is oriented away from the Ca^{2+} binding site, and we
367 detect weak density only for the bottom Ca^{2+} binding site (Fig. 5f, i and Extended Data Fig. 9l),
368 suggesting impaired ion binding. Thus, the A444P mutation impairs scrambling, and favors states
369 with short or bent TM6, with weakened Ca^{2+}-binding. These results suggest that the Ca^{2+}-
370 dependent straightening of TM6 might be important for closed groove scrambling. It is likely that
371 the contribution of the TM6 rearrangements to scrambling are smaller than those of groove
372 opening. Therefore, their effects are revealed only in conditions favoring closed groove scrambling.
373
374 **The effect of nhTMEM16 mutants depends on the lipid environment**
375 Finally, we note that our results on R432A nhTMEM16 contrast with our previous report [27], where
376 we showed that this and several other mutations, such as Y439A, greatly impair nhTMEm16
377 scrambling activity. The key difference between our current and past experiments is the membrane
378 composition, a DOPC/DOPG mixture here and a POPE/POPG/Egg PC mixture then. To test if
379 changes in lipid headgroups or acyl chain saturation underlie this difference we reconstituted WT

380 and mutant nhTMEM16 in liposomes formed from DOPC/DOPG, POPE/POPG, DOPE/DOPG
381 and POPC/POPG lipid mixtures. Consistent with previous reports [27,37], WT nhTMEM16 is active
382 in all compositions, with a ~3-fold reduction in POPE/POPG membranes compared to the other
383 conditions (Fig. 6a, d and e). In contrast, scrambling by R432A nhTMEM16 is reduced by >200-
384 fold in POPE/POPG liposomes, but is WT-like in DOPC/DOPG, DOPE/DOPG and POPC/POPG
385 membranes (Fig. 6b, d and e). The Y439A mutant is also only inhibited in POPE/POPG liposomes
386 and WT-like in the others (Fig. 6c-e). Thus, scrambling activity is specifically reduced in POPE-
387 containing membranes, as all constructs are functional in DO lipids as well as in PO membranes
388 formed from PC/PG mixtures. This rules out specific interactions between the protein and the PE
389 headgroup or the 16:1-18:0 acyl chains of PO lipids. While we do not have a satisfactory
390 explanation for this observation, we note that the transition temperature (T_m) of POPE membranes
391 is close to room temperature, whereas those of all other tested lipids is < 0 ºC [42]. This raises the
392 possibility that scrambling might be sensitive to the formation of local gel-like microdomains with
393 reduced fluidity. This finding underscores the importance of the membrane environment in
394 assaying the activity of TMEM16 scramblases.

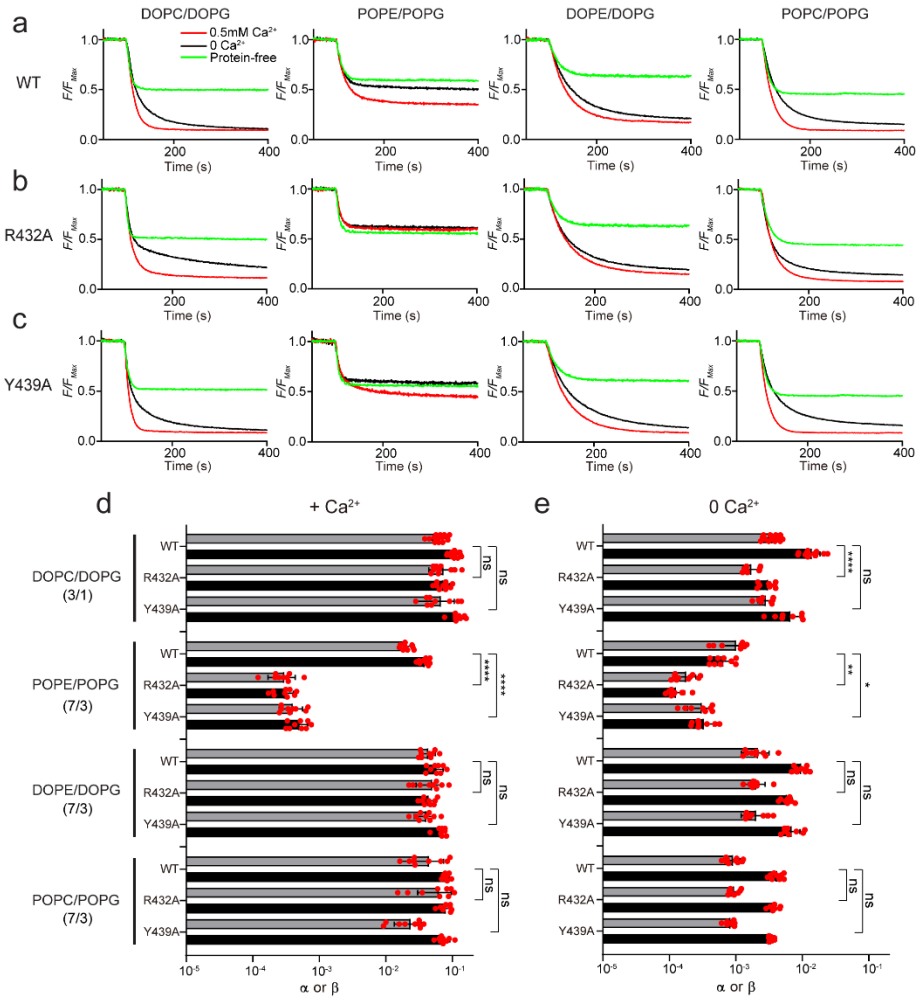

Figure 6. The lipid environment determines the effect of mutations of nhTMEM16. a-c, Representative traces of the dithionite induced fluorescence decay in the scrambling assay in protein-free liposomes (green) or proteoliposomes reconstituted with WT (**a**), R432A (**b**) or Y432A (**c**) nhTMEM16 in the presence (red) and absence (black) of Ca^{2+}. Liposomes were formed from a 3:1 mix of DOPC/DOPG, or a 7:3 mix of POPE/POPG, DOPE/DOPG and POPC/POPG lipids. **d-e,** Forward (α) and reverse (β) scrambling rate constants of WT, R423A and Y439A nhTMEM16 in the four different lipid compositions (as in **a-c**) in the presence of 0.5 mM (**d**) or 0 Ca^{2+} (**e**). Bars are averages for α (black) and β (gray) (N ⩾ 3), error bars are S. Dev., and red circles are values from individual repeats. The statistical significance of the effects of the mutants on the scrambling rate constants was evaluated with a two-sided Student's t-test with a Bonferroni correction. *, **, and **** respectively denote $p<5\cdot10^{-3}$, $<10^{-3}$, and $<10^{-5}$ after Bonferroni correction.

Discussion

The Ca^{2+} dependent activation of TMEM16 scramblases plays a critical role in a variety of cellular signaling pathways [1-3,6]. Despite extensive structural and functional investigations, the structural basis of their Ca^{2+}-dependent activation and lipid transport mechanisms remain poorly understood. For example, TMEM16 activation is thought to entail opening of a hydrophilic groove following Ca^{2+} binding to a site formed by residues in the TM6-TM8 helices. However, it is not clear how

413 Ca^{2+} binding facilitates the displacement of TM4 to open the groove. Further, while an open groove
414 facilitates scrambling, the closed groove has also been proposed to be scrambling competent [19,30].
415 However, the structural basis of lipid scrambling outside a closed groove remain unknown.
416 Our high-resolution structures of Ca^{2+}-bound closed nhTMEM16 reconstituted into lipid
417 nanodiscs allowed us to directly visualize how lipid molecules interact with the closed groove of
418 the scramblase (Fig. 2a-d; Supplementary Video 1 and Extended Data Fig. 6). We found that inner
419 and outer leaflet lipids adopt distorted poses where their phosphate headgroups coming within ~27
420 Å of each other at the closed groove. This arrangement of the lipids results in a ~30% thinning of
421 the hydrocarbon core of the membrane which will facilitate scrambling when the groove is closed.
422 Mutants aimed at disrupting this lipid arrangement only impair scrambling by nhTMEM16 in the
423 absence of Ca^{2+}, when the groove is closed, but have no effect in the presence of Ca^{2+}, when the
424 groove can open (Fig. 3h, i). These observations suggest that the observed distortion of the lipids
425 near the groove, and the ensuing membrane thinning, are critical for closed groove scrambling.
426 We speculate this mechanism is likely conserved across TMEM16 scramblases for several reasons.
427 First, mutations at similar positions also impair closed groove scrambling in afTMEM16 [30]. Second,
428 the membrane near the closed groove of afTMEM16 and TMEM16F is thinned to a similar extent
429 to what we see here for nhTMEM16 [19,21,30] and, third, in TMEM16K two resolved detergent
430 molecules adopt tilted poses similar to those of the P4 and P8 lipids in nhTMEM16 [18] (Extended
431 Data Fig. 10a-c). These results suggest that membrane thinning could be a general and
432 evolutionary conserved mechanism for lipid scrambling by the TMEM16s, although with different
433 details among homologues. With a closed groove, thinning is less pronounced, and scrambling is
434 slower than when the groove is open, rationalizing the Ca^{2+} dependence of TMEM16 activity
435 (Extended Data Fig. 10d-f). The strong dependence of closed groove scrambling on membrane
436 properties could provide a mode of regulation of TMEM16 activity in cellular membranes, such
437 as the cholesterol rich plasma membrane or the thinner ER membrane. In sum, our work [17,30],
438 together with that of others [19,21,22,29,31], suggest that the TMEM16 proteins provide a delocalized,
439 low-energy path for lipids to traverse the membrane, rather than forming discrete binding sites that
440 the lipids move between. Mutations aimed at disrupting protein-lipid interactions near an open or
441 closed groove leave scrambling unaltered [30] or cause less than a tenfold reduction in activity (Fig.
442 3), respectively. Thus, while the membrane distortion imposed by these protein-lipid interactions

443 is critical for scrambling, it is possible that the transported lipids might not be the ones visualized
444 to directly interact with the protein.

445 Piecing together our results with past work [7,21] we can provide a detailed description of the
446 molecular transitions underlying the Ca^{2+} dependent activation of nhTMEM16 (Supplementary
447 Video 2). To this end, we make two plausible assumptions: that the previously reported state
448 obtained in Ca^{2+}-free conditions corresponds to a partially bound state and, that the 7 known
449 conformations of nhTMEM16, reported here and earlier [21], represent intermediates along the
450 transition from apo closed to Ca^{2+} bound open. The relative stability of these conformations might
451 be differentially affected by the membrane environment, which would result in slightly different
452 opening trajectories. Nonetheless, we hypothesize that these states are visited -albeit briefly-
453 during opening. Starting in the apo conformation the groove is closed, TM6 is bent, and the
454 cytosolic domains are apart (PDBID: 8TPM) (Fig. 1a, f). Partial occupancy of the Ca^{2+} sites
455 promotes a movement of the cytosolic domains away from the symmetry axis and a partial
456 straightening of TM6 (PDBID: 6QM4) (Extended Data Fig. 5a, e and g). Binding of both Ca^{2+}
457 ions favors the compete straightening of TM6 and the formation of the intracellular π-helix turn,
458 which allows the acidic side chain of E452 on TM6 to come within coordination distance of the
459 bound ion (PDBID: 8TOI) (Fig. 1b, g, 4a and Extended Data Fig. 7f). These rearrangements
460 weaken the TM4-TM6 packing, allowing TM4 to move and adopt the intermediate-closed (PDBID:
461 6QMA) and intermediate-open configurations (PDBID: 8TPN) (Fig. 1d, i), which might lead to
462 the formation of ion conduction pores (Fig. 1n, o). The partial disengagement of the TM4 from
463 TM6 allows the extracellular portion of TM6 between the bound Ca^{2+} ions and the R432-E313 salt
464 bridge to rotate, resulting in the formation of a second π-helix turn at A444 (Fig. 4b). These
465 rearrangements disrupt the TM4-TM6 interface, and likely facilitate the transition to
466 conformations with an open groove (PDBID: 8TOL and 8TOK) (Fig. 1c, e, h and j). The role of
467 the R432-E313 salt bridge in groove opening is supported by our finding that the R432A mutation
468 stabilizes the Ca^{2+}-bound closed conformation in nhTMEM16 (Fig. 4c-f). This interaction between
469 TM6 and TM3 is well conserved across fungal and mammalian TMEM16 homologues (Extended
470 Data Fig. 10g-j). Interestingly, in mTMEM16F the interaction is present, but the charges are
471 reversed, and the closed groove is the most favored conformation [19,22]. Similarly, charge-reversal
472 mutants of nhTMEM16 are non-functional in POPE-containing liposomes [27], suggesting that the
473 precise arrangement of charges in the salt bridge is also important.

Our results reveal that the environment plays a critical role in determining the structures of nhTMEM16 conformations as well as the population distribution among them. Indeed, subtle changes in lipid composition, from PO to DO lipids, and/or nanodisc scaffold proteins, from MSP1E3 to MSP2N2, can affect ion binding, protein conformations, and their distributions. Specifically, in MSP1E3 DOPC/DOPG nanodiscs nhTMEM16 can adopt an apo conformation (Fig. 1a, f and Extended Data Fig. 5d) which differs from the previously reported one in MSP2N2 POPC/POPG nanodiscs because of conformational rearrangements in the cytosolic and groove regions (Extended Data Fig. 5c). These differences likely reflect the different occupancy of the Ca^{2+} sites, empty in our structure but partially occupied by an unknown ligand in the previous [21] one (Extended Data Fig. 5e). This suggests that the membrane environment might modulate TMEM16 activity by affecting ion binding, as both structures were obtained in similar Ca^{2+} buffering conditions. Structural differences are also observed in the conformations adopted in the MSP2N2 DOPC/DOPG nanodiscs compared to those seen in MSP2N2 POPC/POPG [21], as both the open and intermediate groove conformations in DO lipids are more open than those seen in PO lipids (Fig. 1l, m and Extended Data Fig. 5i, j). Indeed, in the intermediate-open conformation seen in DO lipids TM4 makes minimal contact with TM6 (Fig. 1n) leading to the formation of a continuous transmembrane pore with internal diameter >4.1 Å, which is sufficiently wide to be fully hydrated and to allow permeation of both chloride and potassium ions. We hypothesize this state could correspond to an ion conductive conformation of nhTMEM16. Unexpectedly, the conformations seen in the smaller MSP1E3 DOPC/DOPG nanodiscs are indistinguishable from those reported in MSP2N2 POPC/POPG, indicating that both nanodisc diameter and lipid properties contribute to stabilizing specific conformations of the protein. Strikingly, these differences in particle distributions, ligand binding state, and conformations do not correlate with changes in activity, as nhTMEM16 scrambles lipids equally well in DOPC/DOPG and POPC/POPG liposomes (Fig. 6), the Ca^{2+}-free conditions are nominally identical (Fig. 1a) [21], and the lipid composition is the same in our MSP1E3 and MSP2N2 reconstitutions (Fig. 1k). Finally, our results suggest that reconstitution in the smaller MSP1E3 nanodiscs favors closed or intermediate conformations of nhTMEM16, as we observe a ~20-fold increase in the fraction of particles with an open groove in the larger MSP2N2 discs (Fig. 1k), where the fraction of particles with a closed groove is undetectable (Fig. 1k). This raises the possibility that unbounded

504 membranes, such as those of liposomes, might perturb less the conformational landscape of the
505 imaged proteins.

506 Recently, much work has been devoted to extracting free energy landscapes of proteins
507 from the analysis of particle distributions in cryoEM imaging experiments [43-48]. Our findings
508 challenge the straightforward assumption that the particle distribution is a faithful reporter of the
509 conformational landscape of the protein. The lack of correspondence between protein activity,
510 particle distribution, and conformation confounds the correlation between the free-energy
511 landscape of a protein, cryoEM particle counts, and activity. Rather, our results show that these
512 distributions also reflect the contributions of the environment, and that even subtle changes in
513 detergent, scaffold protein, or lipid constituents of nanodiscs can shift the preferred conformations
514 adopted by the reconstituted protein. Our results suggest that the energetic contributions of these
515 environmental factors could be relatively small, in the 1-3 kCal Mol^{-1} range. Nonetheless, their
516 effects can profoundly affect the interpretation of structural experiments such as the identification
517 of dominant conformations in a sample (Fig. 1k) or in the assignment of functional properties to a
518 specific conformation (Fig. 1o). These effects should be evaluated for each protein system under
519 consideration, as for example whereas the conformational landscape of WT nhTMEM16 is highly
520 sensitive to the environment, that of its close homologues afTMEM16 or mTMEM16F is not
521 [17,19,22,30], and even the single point mutant R432A nhTMEM16 exclusively adopts only one
522 conformation in different nanodisc scaffolds (Fig. 4c-f). Interestingly, a recent report suggests that
523 the conformational landscape of the pentameric ligand gated ion channel ELIC is also affected by
524 subtle changes in the imaging environment [49], suggesting these considerations are generally
525 applicable to diverse types of membrane proteins. It will be interesting to see whether structures
526 determined in unbounded membranes, such as liposomes will differ from those determined in
527 nanodiscs or detergent systems.
528

529 **Data availability**

530 The data that support this study are available from the corresponding author upon request. All
531 models and associated cryoEM maps have been deposited into the Electron Microscopy Data Bank
532 (EMDB) and the Protein Data Bank (PDB). The depositions include final maps, unsharpened maps,
533 local refined maps, and associated FSC curves. Accession codes are listed here and in Table 1. WT
534 nhTMEM16 in MSP1E3 nanodiscs in the absence of Ca^{2+}: EMD-41477 and PDB 8TPM; WT
535 nhTMEM16 in MSP1E3 nanodiscs in the presence of Ca^{2+} (closed state): EMD-41453, EMD-
536 41457 (consensus map), EMD-41458 (monomer map) and PDB 8TOI; WT nhTMEM16 in
537 MSP1E3 nanodiscs in the presence of Ca^{2+} (open state): EMD-41455 and PDB 8TOL; WT
538 nhTMEM16 in MSP2N2 nanodiscs in the presence of Ca^{2+} (intermediate-open state): EMD-
539 41478 and PDB 8TPN; WT nhTMEM16 in MSP2N2 nanodiscs in the presence of Ca^{2+} (open
540 state): EMD-41454 and PDB 8TOK; R432A nhTMEM16 in MSP1E3 nanodiscs in the presence
541 of Ca^{2+} (closed state): EMD-41479 and PDB 8TPO; R423A nhTMEM16 in MSP2N2 nanodiscs
542 in the presence of Ca^{2+} (closed state): EMD-41480 and PDB 8TPP; A444P nhTMEM16 in
543 MSP1E3 nanodiscs in the presence of Ca^{2+}: EMD-41481 and PDB 8TPQ for the closed state with
544 long TM6, EMD-41482 and PDB 8TPR for the closed state with short TM6, EMD-41483 and
545 PDB 8TPS for the closed state with bent TM6, EMD-41484 and PDB 8TPT for the closed state
546 with asymmetric TM6 (long TM6/short TM6).

547

548 **Acknowledgements**

549 The authors thank members of the Accardi lab, Harel Weinstein and George Khelashvili for helpful
550 discussions and suggestions. The work was supported by National Institutes of Health (NIH) grants
551 R01GM106717 and 1R35GM152012 (to A.A.). Some of this work was performed at the Simons
552 Electron Microscopy Center and National Resource for Automated Molecular Microscopy located
553 at the New York Structural Biology Center, supported by grants from the Simons Foundation
554 (SF349247), NYSTAR, and the NIH National Institute of General Medical Sciences (GM103310).
555 Part of the work was performed at NYU Langone Health's Cryo-Electron Microscopy Laboratory
556 (RRID: SCR_019202) with the help of Dr. Bing Wang and Dr. William Rice, and at the Cryo-EM
557 Core Facility at Weill Cornell Medical College with the help of Dr. Carl Fluck. Initial screening
558 was performed at NYU Langone Health's Cryo-Electron Microscopy Laboratory (RRID:
559 SCR_019202) and the Cryo-EM Core Facility at Weill Cornell Medical College.

Author contributions

Z.F. and A.A. designed the experiments; Z.F. and O.E.A. performed experiments; Z.F., O.E.A., and A.A. analyzed the data; Z.F. and A.A. wrote the paper. All authors edited the manuscript.

Competing Interests statement

The authors declare no competing interests.

570 **References**

571 1 Whitlock, J. M. & Hartzell, H. C. Anoctamins/TMEM16 Proteins: Chloride Channels Flirting
572 with Lipids and Extracellular Vesicles. *Annu Rev Physiol* **10**, 119-143 (2017).
573 2 Bevers, E. M. & Williamson, P. L. Getting to the Outer Leaflet: Physiology of
574 Phosphatidylserine Exposure at the Plasma Membrane. *Physiol Rev* **96**, 605-645 (2016).
575 https://doi.org/10.1152/physrev.00020.2015
576 3 Sakuragi, T. & Nagata, S. Regulation of phospholipid distribution in the lipid bilayer by
577 flippases and scramblases. *Nature Reviews Molecular Cell Biology* (2023).
578 https://doi.org/10.1038/s41580-023-00604-z
579 4 Suzuki, J., Umeda, M., Sims, P. J. & Nagata, S. Calcium-dependent phospholipid scrambling
580 by TMEM16F. *Nature* **468**, 834-838 (2010).
581 5 Malvezzi, M. *et al.* Ca2+-dependent phospholipid scrambling by a reconstituted TMEM16
582 ion channel. *Nature Communications* **4**, 2367 (2013).
583 https://doi.org/10.1038/ncomms3367
584 6 Falzone, M., Malvezzi, M., Lee, B. C. & Accardi, A. Known structures and unknown
585 mechanisms of TMEM16 scramblases and channels. *JGP* **150**, 933-947 (2018).
586 https://doi.org/doi: 10.1085/jgp.201711957
587 7 Brunner, J. D., Lim, N. K., Schenck, S., Duerst, A. & Dutzler, R. X-ray structure of a calcium-
588 activated TMEM16 lipid scramblase. *Nature* **516**, 207-212 (2014).
589 8 Suzuki, J., Denning, D. P., Imanishi, E., Horvitz, H. R. & Nagata, S. Xk-Related Protein 8 and
590 CED-8 Promote Phosphatidylserine Exposure in Apoptotic Cells. *Science* **341**, 403-406
591 (2013). https://doi.org/10.1126/science.1236758
592 9 Matoba, K. *et al.* Atg9 is a lipid scramblase that mediates autophagosomal membrane
593 expansion. *Nat Struct Mol Biol* **27**, 1185-1193 (2020). https://doi.org/10.1038/s41594-
594 020-00518-w
595 10 Maeda, S. *et al.* Structure, lipid scrambling activity and role in autophagosome formation
596 of ATG9A. *Nat Struct Mol Biol* **27**, 1194-1201 (2020). https://doi.org/10.1038/s41594-
597 020-00520-2
598 11 Guardia, C. M. *et al.* Structure of Human ATG9A, the Only Transmembrane Protein of the
599 Core Autophagy Machinery. *Cell Rep* **31**, 107837 (2020).
600 https://doi.org/10.1016/j.celrep.2020.107837
601 12 Menon, I. *et al.* Opsin is a phospholipid flippase. *Curr Biol* **21**, 149-153 (2011).
602 https://doi.org/10.1016/j.cub.2010.12.031
603 13 Jahn, H., Bartoš, L., Holthuis, J. C. M., Vácha, R. & Menon, A. K. Mitochondrial phospholipid
604 import mediated by VDAC, a dimeric beta barrel scramblase. *bioRxiv*,
605 2022.2010.2017.512472 (2022). https://doi.org/10.1101/2022.10.17.512472
606 14 Anglin, T. C., Brown, K. L. & Conboy, J. C. Phospholipid Flip-flop Modulated by
607 Transmembrane Peptides WALP and Melittin. *Journal of structural biology* **168**, 37-52
608 (2009). https://doi.org/10.1016/j.jsb.2009.06.001
609 15 Mihajlovic, M. & Lazaridis, T. Antimicrobial Peptides in Toroidal and Cylindrical Pores.
610 *Biochimica et biophysica acta* **1798**, 1485-1493 (2010).
611 https://doi.org/10.1016/j.bbamem.2010.04.004

612 16 Kol, M. A. *et al.* Phospholipid flop induced by transmembrane peptides in model
613 membranes is modulated by lipid composition. *Biochemistry* **42**, 231-237 (2003).
614 https://doi.org/10.1021/bi0268403
615 17 Falzone, M. E. *et al.* Structural basis of Ca(2+)-dependent activation and lipid transport by
616 a TMEM16 scramblase. *Elife* **8** (2019). https://doi.org/10.7554/eLife.43229
617 18 Bushell, S. R. *et al.* The structural basis of lipid scrambling and inactivation in the
618 endoplasmic reticulum scramblase TMEM16K. *Nature Communications* **10**, 3956 (2019).
619 https://doi.org/10.1038/s41467-019-11753-1
620 19 Feng, S. *et al.* Cryo-EM Studies of TMEM16F Calcium-Activated Ion Channel Suggest
621 Features Important for Lipid Scrambling. *Cell Reports* **28**, 567-579.e564 (2019).
622 https://doi.org/10.1016/j.celrep.2019.06.023
623 20 Straub, M. S., Alvadia, C., Sawicka, M. & Dutzler, R. Cryo-EM structures of the caspase-
624 activated protein XKR9 involved in apoptotic lipid scrambling. *eLife* **10**, e69800 (2021).
625 https://doi.org/10.7554/eLife.69800
626 21 Kalienkova, V. *et al.* Stepwise activation mechanism of the scramblase nhTMEM16
627 revealed by cryo-EM. *eLife* **8**, e44364 (2019). https://doi.org/10.7554/eLife.44364
628 22 Alvadia, C. *et al.* Cryo-EM structures and functional characterization of the murine lipid
629 scramblase TMEM16F. *eLife* **8**, e44365 (2019). https://doi.org/10.7554/eLife.44365
630 23 Pomorski, T. & Menon, A. K. Lipid flippases and their biological functions. *Cell Mol Life Sci*
631 **63**, 2908-2921 (2006).
632 24 Bethel, N. P. & Grabe, M. Atomistic insight into lipid translocation by a TMEM16
633 scramblase. *Proc Natl Acad Sci USA* **113**, 14049-14054 (2016).
634 25 Jiang, T., Yu, K., Hartzell, H. C. & Tajkhorshid, E. Lipids and ions traverse the membrane by
635 the same physical pathway in the nhTMEM16 scramblase. *Elife* **6** (2017).
636 https://doi.org/10.7554/eLife.28671
637 26 Yu, K. *et al.* Identification of a lipid scrambling domain in ANO6/TMEM16F. *eLife* **4**, 1-23
638 (2015). https://doi.org/10.7554/eLife.06901
639 27 Lee, B. C. *et al.* Gating mechanism of the extracellular entry to the lipid pathway in a
640 TMEM16 scramblase. *Nat Commun* **9**, 3251 (2018). https://doi.org/10.1038/s41467-018-
641 05724-1
642 28 Kostritskii, A. Y. & Machtens, J.-P. Molecular mechanisms of ion conduction and ion
643 selectivity in TMEM16 lipid scramblases. *Nature Communications* **12**, 2826 (2021).
644 https://doi.org/10.1038/s41467-021-22724-w
645 29 Arndt, M. *et al.* Structural basis for the activation of the lipid scramblase TMEM16F. *Nat*
646 *Commun* **13**, 6692 (2022). https://doi.org/10.1038/s41467-022-34497-x
647 30 Falzone, M. E. *et al.* TMEM16 scramblases thin the membrane to enable lipid scrambling.
648 *Nat Commun* **13**, 2604 (2022). https://doi.org/10.1038/s41467-022-30300-z
649 31 Feng, S. *et al.* Identification of a drug binding pocket in TMEM16F calcium-activated ion
650 channel and lipid scramblase. *Nature Communications* **14**, 4874 (2023).
651 https://doi.org/10.1038/s41467-023-40410-x
652 32 Ritchie, T. K. *et al.* in *Methods in Enzymology* (Elsevier Masson SAS, 2009).
653 33 Grinkova, Y. V., Denisov, I. G. & Sligar, S. G. Engineering extended membrane scaffold
654 proteins for self-assembly of soluble nanoscale lipid bilayers. *Protein Engineering, Design*
655 *and Selection* **23**, 843-848 (2010).

656 34 Lim, N. K., Lam, A. K. M. & Dutzler, R. Independent activation of ion conduction pores in
657 the double-barreled calcium-activated chloride channel TMEM16A. *JGP* **148**, 375-392
658 (2016). https://doi.org/10.1085/jgp.201611650
659 35 Jeng, G., Aggarwal, M., Yu, W.-P. & Chen, T.-Y. Independent activation of distinct pores in
660 dimeric TMEM16A channels. *The Journal of General Physiology* **148**, 393-404 (2016).
661 https://doi.org/10.1085/jgp.201611651
662 36 Khelashvili, G. *et al.* Dynamic modulation of the lipid translocation groove generates a
663 conductive ion channel in Ca2+-bound nhTMEM16. *Nature Communications* **10**, 4972
664 (2019). https://doi.org/10.1038/s41467-019-12865-4
665 37 Lee, B.-C., Menon, Anant K. & Accardi, A. The nhTMEM16 Scramblase Is Also a
666 Nonselective Ion Channel. *Biophysical Journal* **111**, 1919-1924 (2016).
667 https://doi.org/10.1016/j.bpj.2016.09.032
668 38 Cheng, X., Khelashvili, G. & Weinstein, H. The permeation of potassium ions through the
669 lipid scrambling path of the membrane protein nhTMEM16. *Frontiers in molecular*
670 *biosciences* **9**, 903972 (2022). https://doi.org/10.3389/fmolb.2022.903972
671 39 Smart, O. S., Neduvelil, J. G., Wang, X., Wallace, B. A. & Sansom, M. S. HOLE: a program
672 for the analysis of the pore dimensions of ion channel structural models. *J Mol Graph* **14**,
673 354-360 (1996).
674 40 Malvezzi, M. *et al.* Out of the groove transport of lipids by TMEM16 and GPCR scramblases
675 *PNAS* (2018). https://doi.org/https://doi.org/10.1073/pnas.1806721115
676 41 Falzone, M. E. & Accardi, A. Reconstitution of Proteoliposomes for Phospholipid
677 Scrambling and Nonselective Channel Assays. *Methods Mol Biol* **2127**, 207-225 (2020).
678 https://doi.org/10.1007/978-1-0716-0373-4_15
679 42 Silvius, J. R., Mak, N. & McElhaney, R. N. Lipid and protein composition and thermotropic
680 lipid phase transitions in fatty acid-homogeneous membranes of Acholeplasma laidlawii
681 B. *Biochim Biophys Acta* **597**, 199-215 (1980). https://doi.org/10.1016/0005-
682 2736(80)90099-1
683 43 Giraldo-Barreto, J. *et al.* A Bayesian approach to extracting free-energy profiles from cryo-
684 electron microscopy experiments. *Scientific reports* **11**, 13657 (2021).
685 https://doi.org/10.1038/s41598-021-92621-1
686 44 Dsouza, R., Mashayekhi, G., Etemadpour, R., Schwander, P. & Ourmazd, A. Energy
687 landscapes from cryo-EM snapshots: a benchmarking study. *Scientific reports* **13**, 1372
688 (2023). https://doi.org/10.1038/s41598-023-28401-w
689 45 Oide, M., Kato, T., Oroguchi, T. & Nakasako, M. Energy landscape of domain motion in
690 glutamate dehydrogenase deduced from cryo-electron microscopy. *The FEBS Journal* **287**,
691 3472-3493 (2020). https://doi.org/https://doi.org/10.1111/febs.15224
692 46 Mashayekhi, G., Vant, J., Polavarapu, A., Ourmazd, A. & Singharoy, A. Energy landscape of
693 the SARS-CoV-2 reveals extensive conformational heterogeneity. *Current Research in*
694 *Structural Biology* **4**, 68-77 (2022).
695 https://doi.org/https://doi.org/10.1016/j.crstbi.2022.02.001
696 47 Frank, J. New Opportunities Created by Single-Particle Cryo-EM: The Mapping of
697 Conformational Space. *Biochemistry* **57**, 888-888 (2018).
698 https://doi.org/10.1021/acs.biochem.8b00064

48 Seitz, E. & Frank, J. POLARIS: Path of Least Action Analysis on Energy Landscapes. *Journal of Chemical Information and Modeling* **60**, 2581-2590 (2020). https://doi.org/10.1021/acs.jcim.9b01108

49 Dalal, V. *et al.* Lipid nanodisc scaffold and size alters the structure of a pentameric ligand-gated ion channel. *bioRxiv*, 2022.2011.2020.517256 (2022). https://doi.org/10.1101/2022.11.20.517256

Methods

Expression and purification of nhTMEM16

Wild-type and mutant nhTMEM16 were expressed using a pYES2 vector with an N-terminal GFP-His_{10}. Expression and purification of all constructs was carried out as described [1,2]. Briefly, *S. cerevisiae* transformed with WT and mutant construct were grown in yeast synthetic drop-out medium supplemented with Uracil (CSM-URA; MP Biomedicals) to an OD_{600} of 0.8 and expression was induced with 2% (w/v) galactose at 25°C for 40 hours. Cells were collected and resuspended in lysis buffer (150 mM NaCl, 50 mM HEPES, pH 7.6) supplemented with 0.5 mM $CaCl_2$, 5 µg ml^{-1} leupeptin, 2 µg ml^{-1} pepstatin and protease inhibitor cocktail tablets (Roche) and lysed with an EmulsiFlex-C3 homogenizer at pressures above 20,000 psi. Cell debris was removed by centrifugation at 3,000 g for 15 min. Membranes were subsequently harvested by centrifugation with a 45 TI rotor (Beckmann) at 200,000 g for 1 hr. Membrane proteins were extracted by supplementing the lysis buffer with 1% n-dodecyl-β-D-maltopyranoside (DDM, Anatrace), and incubated for 1.5 h at 4°C. The insoluble fraction was removed by centrifugation at 30,000 g for 30 min. The supernatant was supplemented with 10 mM imidazole, loaded onto a column of Ni-NTA agarose resin (Qiagen), washed with 150 mM NaCl, 5% (w/v) glycerol, 0.5 mM $CaCl_2$, 10 mM HEPES, pH 7.6 and 0.025% DDM (Buffer A) + 50 mM imidazole and eluted with Buffer A + 400 mM imidazole. The nhTMEM16 protein peak was collected and concentrated using a 100 kDa molecular weight cut off concentrator (Amicon Ultra, Millipore). The N-terminal GFP-His_{10} tag was cleaved overnight with 3C protease before gel filtration chromatography by using a Sepharose 6 Increase 10/300 GL column (GE Healthcare). For the purification of apo proteins, 2 mM EGTA was used in all steps.

Liposome reconstitution

Liposomes were prepared as described [2]. A 3:1 mixture of 1-palmitoyl-2-oleoyl-snglycero-3-phosphoethanolamine (POPE) and 1-palmitoyl-2-oleoyl-sn-glycero-3-phospho-(1′-rac-glycerol) (POPG) was used for the preparation of POPE:POPG liposomes and a 7:3 mixture of 1,2-dioleoyl-sn-glycero-3-phosphocholine (DOPC) and 1,2-dioleoyl-sn-glycero-3-phospho-(1'-rac-glycerol) (DOPG) was used for the preparation of DOPC:DOPG liposomes. For the preparation of DOPE:DOPG and POPC:POPG liposomes, a 7:3 mixture of 1,2-dioleoyl-sn-glycero-3-phosphoethanolamine (DOPE) and DOPG and 1-palmitoyl-2-oleoyl-glycero-3-phosphocholine

(POPG) and POPG were used, respectively. Briefly lipids in chloroform (Avanti), including 0.4% w/w 1-myristoyl-2-{6-[(7-nitro-2-1,3-benzoxadiazol-4-yl)amino]hexanoyl}-sn-glycero-3-phosphoethanolamine (NBD-PE), were dried under nitrogen gas. The dried lipids were washed with pentane and resuspended at 20 mg ml^{-1} in 150 mM KCl, 50 mM HEPES pH 7.4 with 35 mM 3-[(3-cholamidopropyl) dimethylammonio]-1-propanesulfonate (CHAPS). The proteins were added at a concentration of 5 µg protein/mg lipids. The detergent was removed by using Bio-Beads SM-2 (Bio-Rad) with rotation at 4 °C. For the mixture without POPE lipids, proteoliposomes were formed by removing the detergent with 5 times Bio-Beads exchanges of 200 mg ml^{-1}. For the mixture with POPE lipids, 4 times Bio-Beads exchanges of 150 mg ml^{-1} were performed. Calcium or EGTA were introduced using sonicate, freeze-thaw cycles. The liposomes were extruded 21 times through a 400-nm membrane before use.

Scrambling assay

The scrambling assay was carried out as described [3]. Briefly, 20 µl of extruded liposomes were added into 2ml of external solution (300 mM KCl, 50 mM HEPES, 0.5 mM $Ca(NO_3)_2$ or 2 mM EGTA, pH 7.4). The fluorescence intensity of the NBD was monitored over time with mixing in a PTI spectrophotometer using excitation and emission wavelengths of 470 and 530 nm. After 100 s recording, sodium dithionite was added at a final concentration of 40 mM. Data was collected using the FelixGX 4.1.0 software at a sampling rate of 3 Hz.

Quantification of scrambling activity

Quantification of the scrambling rate constants by nhTMEM16 was determined as described [2,3]. Briefly, the fluorescence time course was fit to the following equation

$$F_{tot}(t) = f_0(L_i^{PF} + (1 - L_i^{PF})e^{-\gamma t}) + \frac{(1-f_0)}{D(\alpha+\beta)}\{\alpha(\lambda_2 + \gamma)(\lambda_1 + \alpha + \beta)e^{\lambda_1 t} + \lambda_1\beta(\lambda_2 + \alpha + \beta + \gamma)e^{\lambda_2 t}\} \quad (1)$$

Where $F_{tot}(t)$ is the total fluorescence at time t, L_i^{PF} is the fraction of NBD-labeled lipids in the inner leaflet of protein free liposomes, where γ is the rate constant of dithionite reduction, f_0 is the

fraction of protein-free liposomes in the sample, α and β are respectively the forward and backward scrambling rate constants and

$$\lambda_1 = -\frac{(\alpha+\beta+\gamma)-\sqrt{(\alpha+\beta+\gamma)^2-4\alpha\gamma}}{2} \quad \lambda_2 = -\frac{(\alpha+\beta+\gamma)+\sqrt{(\alpha+\beta+\gamma)^2-4\alpha\gamma}}{2}$$

$$D = (\lambda_1 + \alpha)(\lambda_2 + \beta + \gamma) - \alpha\beta$$

The free parameters of the fit are f_0, α and β while L_i^{PF} and γ are experimentally determined from experiments on protein-free liposomes. In protein-free vesicles a very slow fluorescence decay is visible, likely reflecting a slow leakage of dithionite into the vesicles or the spontaneous flipping of the NBD-labeled lipids. A linear fit was used to estimate that the rate of this process is L = $(5.4\pm1.6)10^{-5}$ s^{-1} (n>160). For wild-type and mutant nhTMEM16 the leak is >2 orders of magnitude smaller than the rate constant of protein-mediated scrambling and therefore is negligible. All conditions were tested side by side with a control preparation.

MSP1E3/MSP2N2 purification and nanodisc reconstitution

MSP1E3 and MSP2N2 were expressed and purified as described [4]. Briefly, MSPs in a pET vector (Addgene #20064 and #29520) was transformed into BL21-Gold (DE3) strain (Stratagene). Transformed cells were grown in LB media supplemented with Kanamycin (50 mg l^{-1}) until reaching an OD_{600} of 0.8. The expression of the proteins was induced by adding 1 mM IPTG (isopropyl β-D-1-thiogalactopyranoside) for 3 hours. The cells were harvested and resuspended a lysis buffer containing 40 mM Tris-HCl pH 8.0, 300 mM NaCl, 1% Triton X-100, 5 μg ml^{-1} leupeptin, 2 μg ml^{-1} pepstatin and protease inhibitor cocktail tablets (Roche). The cells were then lysed by sonication and cell debris was removed by centrifugation at 30,000 g for 45 min at 4° C. The supernatant was incubated with Ni-NTA agarose resin for one hour at 4 °C. The resin was then sequentially washed with 40 mM Tris-HCl pH 8.0 and 300 mM NaCl (Buffer B) + 1% Triton X-100; followed by a wash with Buffer B + 50 mM sodium cholate, 20 mM imidazole; and one with Buffer B + 50 mM imidazole. The protein was eluted with buffer B + 400 mM imidazole. The eluted protein was further purified by gel filtration chromatography using a Superdex 200 Increase 10/300 GL column (GE Lifesciences) pre-equilibrated with buffer C (150 mM KCl, 50 mM Tris pH 8.0) supplemented with 0.5 mM EDTA. The final protein was concentrated to ~10 mg ml^{-1} using a 30 kDa molecular weight cut-off concentrator (Amicon Ultra, Millipore). The concentrated protein was flash-frozen and stored at -80 °C until further use.

Reconstitution of nhTMEM16 in nanodiscs was carried out as described [5]. 7DOPC:3DOPG lipids in chloroform (Avanti) were dried under nitrogen gas, washed with pentane, and resuspended in buffer C and 40 mM sodium cholate (Anatrace) at a final lipid concentration of 20 mM. Molar ratios of 1:0.8:60 for MSP1E3:nhTMEM16:lipids and 1:0.8:150 for MSP2N2:nhTMEM16:lipids were mixed at a final lipid concentration of 7 mM and incubated at room temperature for 20 minutes. Detergent removal was carried out at 4ºC via incubation with Bio-Beads SM-2 (Bio-Rad) at a concentration of 200 mg ml^{-1} for three times with two hours for each time. After reconstitution, the mixture containing the nhTMEM16-containing nanodiscs was subjected to purification using a Superose 6 Increase 10/300 GL column (GE Lifesciences) pre-equilibrated with 50 mM HEPES pH 8.0 150 mM KCl plus 0.5 mM $CaCl_2$ or 5 mM EGTA and the peak corresponding to nhTMEM16-containing nanodiscs was collected for cryo-electron microscopy analysis.

Grid preparation and data collection

3.5 uL of nhTMEM16-containing nanodiscs (3-7mg ml^{-1}) supplemented with 1.5 or 3 mM Fos-Choline-8-Fluorinated (Anatrace) was applied to a glow-discharged UltrAuFoil R1.2/1.3 300-mesh gold grid (Quantifoil) and incubated for one minute under 100% humidity at 15°C. Following incubation, grids were blotted for 2 s and plunge frozen in liquid ethane using a Vitrobot Mark IV (FEI). Sample grids were screened and collected on a 300kV Titan Krios microscope (Thermo Fisher Scientific) equipped with a K3 direct detection camera (Gatan) at NYU Langone Health's Cryo-Electron Microscopy Laboratory or 200kV Glacios microscope with a Falcon4i direct detection camera (Thermo Fisher Scientific) at the Cryo-EM Core Facility at Weill Cornell Medical College. Energy filter (either from Gatan or Thermo Fisher Scientific) set to a slit width of 20 eV was used in data collection. For additional parameters, see Table 1.

Image processing

All datasets were processed using Relion 3.1 or Relion 4.0 [6]. Motion correction was performed using MotionCorr2 [6] and contrast transfer function (CTF) estimation was carried out using CTFFIND4 [7] via Relion. A 2x binning was applied for motion correction in all datasets. Particle picking was conducted using a 3D volume of the nhTMEM16-nanodisc complex low-pass filtered to 20 Å. For all datasets, 2-3 rounds of 2D classification were performed to select particles that

displayed structural features resembling the nhTMEM16-nanodisc complex. The selected particles underwent several iterations of 3D refinement and 3D classification, with or without alignment, to identify potential alternate conformations. Particles sorted into the same conformation were combined and subjected to 3D refinement followed by several rounds of CTF refinement [6] and Bayesian polishing [8]. All 3D refinements in Relion were conducted initially without a mask, and the converged refinement was continued with a mask excluding the nanodisc. In reconstructions where no conformational heterogeneity was observed between two protomers, C2 symmetry was applied during 3D refinement to further enhance resolution. The final resolution of all maps was determined using the gold-standard Fourier shell correlation (FSC) = 0.143 criterion and applying a soft mask around the protein using Relion Postprocessing. Density modification was applied to some final reconstructions to facilitate model building by using two unfiltered half-maps with a soft mask in Phenix v1.20.1-4487 [9,10]. Local resolution estimation for all final maps was performed using Relion. The processing strategy described here was applied to all datasets, with adaptations made for specific datasets as described below.

For wild type nhTMEM16 in the MSP1E3/+Ca^{2+} dataset, conformational heterogeneity of the groove was initially detected in 3D classifications at an early stage. 3D classes with strong and well-defined density for the closed groove were pooled and separately processed from those with poorly defined density for TM3 and TM4. The combined particles with same closed conformation were subjected to the processing strategy described above. The homogenous subset of 1,017,312 particles was used for the final 3D reconstruction, resulting in a 2.64 Å reconstruction in C2 symmetry. To achieve a better reconstruction of individual lipids, the final subset of dimeric particles was subjected to symmetry expansion and signal subtraction of individual protomers followed by 3D classification with a monomer mask on the expanded monomers. One subset containing 875,283 monomers showed strong density for lipids was selected. Local refinement followed by density modification on these particles, yielded a 2.64 Å reconstruction of the monomer. Two copies of locally refined monomers were aligned on the initial C2 dimer map and merged in Chimera using "vop maximum" command to obtain the final map. This map was used for the model building of lipids and protein. For data processing of the open state, classes with poorly defined TM3 and TM4 conformation were pooled and subjected to 5 rounds of 3D classification without alignment using a dimer mask that excluded the nanodisc density. Particles presenting the same conformation in all 5 runs were extracted using the Starparser v1.38 script

(https://github.com/sami-chaaban/starparser). The resulting 55,830 particles in the open state were subjected to 3D refinement with C2 symmetry applied, resulting in a 2.85 Å reconstruction. To identify dimers with the groove in different states, symmetry expansion and single subtraction were carried out on the initially separated subset with poorly defined TM3 and TM4 and followed by 3D classification with a monomer mask on the expanded monomers. Monomers in the open or closed state were reverted to original particles and the particles present in both subsets were sorted out, resulting in 21,677 particles. 3D auto-refinement of this subset lead to a 3.40 Å reconstruction with the groove open in one protomer and closed in the other. A similar image processing strategy was also applied to the wild-type in MSP2N2/+Ca^{2+} dataset to identify the intermediate-open and open conformations.

For wild type nhTMEM16 in the MSP1E3/0 Ca^{2+} dataset, the TM6 in the final map was poorly resolved, suggesting high conformational mobility, which impeded precise model building of this region. To improve the interpretability of the map for TM6, symmetry expansion and signal subtraction followed by 3D classification were carried out with a monomer mask on a subset of 643,398 particles. This resulted in a subset of 540,140 monomers that showed strong density for TM6. 3D refinement of this subset yielded a monomer reconstruction with improved quality of TM6. A composite map was generated by merging two copies of the monomer map with the C2 dimer map using the "vop maximum" command in Chimera. This composite map further assisted in the model building of TM6.

For the A444P MSP1E3/+Ca^{2+} dataset, conformational heterogeneity of TM6 was detected in 3D classifications after the initial rounds of classification. To identify alternate conformations, the maps for individual protomers were isolated using symmetry expansion and signal subtraction. Several rounds of 3D classifications without alignment were performed using a mask only for TM1-2/5-9 on the signal subtracted protomers which yielded a subset of 388,135 particles. This resulted in a subset of monomers with TM6 in a bent conformation and Ca^{2+} density only at the lower site. The 3D reconstruction of this subset was used as a reference in subsequent masked 3D classifications, resulting in a total number of 140,913 protomers in the bent conformation. This subset of protomers was reverted to the original dimer particles, followed by the removal of duplicated particles, resulting in a subset of 17,404 particles. 3D refinement with C2 symmetry applied resulted in a 2.97 Å reconstruction. 3D classifications without alignment were also

performed using a mask only for TM6-8 on the same set of signal subtracted protomers. This resulted in two subsets of protomers with distinct TM6 conformation and Ca^{2+} occupancy. One subset had a long TM6 with strong density for two Ca^{2+} sites (10.1%), and the other subset had a short TM6 with weaker density for the upper Ca^{2+} site (80.8%). These two subsets were separately selected and reverted to the original dimer particles. After removing duplicated particles, 3D refinement with C2 symmetry was carried out on the long TM6 subset, yielding a final reconstruction at 3.35 Å. For the reconstruction of the short TM6, the subset of 253,803 particles was further cleaned up by removing particles in the bent TM6 conformation. This resulted in a final subset of 174,312 particles. 3D refinement of this subset led to a 2.85 Å reconstruction with C2 symmetry applied. A similar strategy used for identifying the open/closed dimers in the wild-type in the MSP1E3/+Ca^{2+} dataset was also applied in this case, resulting a 3.01 Å reconstruction of an A444P dimer with one protomer with a long TM6 and the other with a short TM6.

Potential additional conformations were carefully examined in all datasets, especially for the wild-type in 0 Ca^{2+}, R432A in MSP1E3/+Ca^{2+} and MSP2N2/+Ca^{2+} datasets that did not display heterogeneity in the initial rounds of 3D classification. We attempted classification with alignment using both global and local searches, with or without a mask excluding the nanodisc. We explored the following approaches: (*i*) varying the low-pass filter (0 to 20 Å), the T parameter (4-64), and the number of classes (4-12); *(ii)* conducting 3D classification without alignment using masks that excluded the nanodisc and varying the same parameters as the classification with alignment; *(iii)* applying symmetry expansion and signal subtraction to isolate the monomers, followed by subsequent focused classification/refinement [11] to account for potential alternate conformations between two protomers; *(iv)* performing classification using cryoSPARC [12] for all the structures described, using particles picked in Relion. In cryoSPARC, we tried 3D variability analysis on all particles selected from 2D classification, as well as on a reduced set of particles sorted using 3D classification in Relion. None of these approaches resulted in the detection of observable protein movements in these datasets.

Model Building and Refinement

Previous nhTMEM16 structures (PDB: 6QMA, 6QMB and 6QM9) were used as starting models and fitted into the new maps using several rounds of PHENIX real space refinement [13]. Lipids

were initially modeled as POPG (PGW) and truncated according to the observed density. In most cases the full headgroup could not be resolved so the lipids were truncated at the phosphate atom. The models were inspected and areas that were better resolved were build *de novo*. The model was improved iteratively by real space refinement in PHENIX [10] imposing crystallographic symmetry and secondary structure restraints. Manual inspection was performed to remove the outliers. In all models, unsharpened maps were used to assist in the building process.

Model validation

To validate the refinement, the FSC between the refined model and the final map was calculated (FSCsum). To evaluate for over-fitting, random shifts of up to 0.3 Å were introduced in the final model and the modified model was refined using PHENIX [10] against one of the two unfiltered half maps. The FSC between this modified-refined model and the half map used in refinement (FSCwork) was determined and compared to the FSC between the modified-refined model and the other half map (FSCfree) which was not used in validation or refinement. The similarity in these curves indicates that the model was not overfit. The quality of all three models was assessed using MolProbity [14] which indicates that the models are of high quality.

References

1 Brunner, J. D., Lim, N. K., Schenck, S., Duerst, A. & Dutzler, R. X-ray structure of a calcium-activated TMEM16 lipid scramblase. *Nature* **516**, 207-212 (2014). https://doi.org/10.1038/nature13984

2 Lee, B. C. *et al.* Gating mechanism of the extracellular entry to the lipid pathway in a TMEM16 scramblase. *Nat Commun* **9**, 3251 (2018). https://doi.org/10.1038/s41467-018-05724-1

3 Malvezzi, M. *et al.* Out-of-the-groove transport of lipids by TMEM16 and GPCR scramblases. *Proc Natl Acad Sci U S A* **115**, E7033-E7042 (2018). https://doi.org/10.1073/pnas.1806721115

4 Ritchie, T. K. *et al.* Chapter 11 - Reconstitution of membrane proteins in phospholipid bilayer nanodiscs. *Methods Enzymol* **464**, 211-231 (2009). https://doi.org/10.1016/S0076-6879(09)64011-8

5 Falzone, M. E. *et al.* Structural basis of Ca(2+)-dependent activation and lipid transport by a TMEM16 scramblase. *Elife* **8** (2019). https://doi.org/10.7554/eLife.43229

6 Zivanov, J. *et al.* New tools for automated high-resolution cryo-EM structure determination in RELION-3. *Elife* **7** (2018). https://doi.org/10.7554/eLife.42166

7 Rohou, A. & Grigorieff, N. CTFFIND4: Fast and accurate defocus estimation from electron micrographs. *Journal of Structural Biology* **192**, 216-221 (2015). https://doi.org/10.1016/j.jsb.2015.08.008

8 Zivanov, J., Nakane, T. & Scheres, S. H. W. A Bayesian approach to beam-induced motion correction in cryo-EM single-particle analysis. *IUCrJ* **6**, 5-17 (2019). https://doi.org/doi:10.1107/S205225251801463X

9 DiMaio, F. *et al.* Improved low-resolution crystallographic refinement with Phenix and Rosetta. *Nat Methods* **10**, 1102-1104 (2013). https://doi.org/10.1038/nmeth.2648

10 Liebschner, D. *et al.* Macromolecular structure determination using X-rays, neutrons and electrons: recent developments in Phenix. *Acta Crystallogr D Struct Biol* **75**, 861-877 (2019). https://doi.org/10.1107/s2059798319011471

11 Paknejad, N. & Hite, R. K. Structural basis for the regulation of inositol trisphosphate receptors by Ca2+ and IP3. *Nature Structural & Molecular Biology* **25**, 660-668 (2018). https://doi.org/10.1038/s41594-018-0089-6

12 Punjani, A., Rubinstein, J. L., Fleet, D. J. & Brubaker, M. A. cryoSPARC: algorithms for rapid unsupervised cryo-EM structure determination. *Nature Methods* **14**, 290 (2017). https://doi.org/10.1038/nmeth.4169

13 Adams, P. D. *et al.* PHENIX: a comprehensive Python-based system for macromolecular structure solution. *Acta Crystallogr D Biol Crystallogr.* **66**, 213-221 (2010).

14 Williams, C. J. *et al.* MolProbity: More and better reference data for improved all-atom structure validation. *Protein science : a publication of the Protein Society* **27**, 293-315 (2018). https://doi.org/10.1002/pro.3330

Cryo-EM data collection, refinement and validation statistics

	WT apo (EMDB-41477) (PDB 8TPM)	WT Ca^{2+}-closed MSP1E3 (EMDB-41453) (PDB 8TOI)	WT Ca^{2+}-open MSP1E3 (EMDB-41455) (PDB 8TOL)	WT Ca^{2+}-intermediate MSP2N2 (EMDB-41478) (PDB 8TPN)	WT Ca^{2+}-open MSP2N2 (EMDB-41454) (PDB 8TOK)	R432A Ca^{2+}-closed MSP1E3 (EMDB-41479) (PDB 8TPO)
Data collection and processing						
Magnification	×105,000	×105,000	×105,000	×130,000	×130,000	×105,000
Voltage (kV)	300	300	300	200	200	300
Electron exposure (e–/Å^2)	58.3	59.4	59.4	30.0	30.0	52.0
Defocus range (μm)	-0.9 to -2.6	-0.9 to -1.9	-0.9 to -1.9	-1.0 to -2.0	-1.0 to -2.0	-0.6 to -2.7
Pixel size (Å)	0.825	0.825	0.825	0..91	0.91	1.082
Symmetry imposed	C2	C2	C2	C2	C2	C2
Micrographs	12,506	13,735	13,735	9,493	9,493	6,409
Initial particle images (no.)	4,885,672	4,574,959	4,574,959	1,948,732	1,948,732	3,613,797
Final particle images (no.)	354,361	1,017,312	55,830	61,965	250,756	390,477
Map resolution (Å)	2.93	2.64	2.85	4.07	3.84	3.59
FSC threshold	0.143	0.143	0.143	0.143	0.143	0.143
Map resolution range (Å)	2.9-3.7	2.7-3.5	3.0-3.8	4.1-4.9	3.7-4.5	3.6-4.4
Refinement						
Initial model used (PDB code)	6QM4	6QMB	6QM9	6QMA	6QM9	6QMB
Model resolution (Å)	3.22	2.83	2.95	4.07	3.84	3.63
FSC threshold	0.5	0.5	0.5	0.5	0.5	0.5
Model resolution range (Å)	3.22-3.70	2.83-3.50	2.95-3.80	4.07-4.90	3.84-4.50	3.63-4.40
Map sharpening *B* factor (Å^2)	-115.0	-109.6	-73.6	-185.4	-191.8	-166.7
Model composition						
Non-hydrogen atoms	10,192	11,414	10,826	8,654	9,908	9,656
Protein residues	1,234	1,298	1,340	1,102	1,258	1,224
Ligands	14	40	16	4	4	8
B factors (Å^2)						
Protein	125.4	77.0	105.5	39.2	32.0	97.3
Ligand	134.5	88.5	112.6	26.6	10.2	88.7
R.m.s. deviations						
Bond lengths (Å)	0.005	0.004	0.003	0.002	0.004	0.005
Bond angles (°)	1.299	1.172	0.620	0.462	0.602	1.304
Validation						
MolProbity score	1.79	1.32	1.74	1.41	1.49	1.79
Clashscore	9.17	2.94	8.74	4.91	4.14	9.10
Poor rotamers (%)	0.69	0	0.37	0	0	0
Ramachandran plot						
Favored (%)	95.70	96.39	96.06	97.19	95.77	95.65
Allowed (%)	4.30	3.61	3.94	2.81	4.23	4.35
Disallowed (%)	0	0	0	0	0	0

	R432A Ca^{2+}-closed MSP2N2 (EMDB-41480) (PDB 8TPP)	A444P Ca^{2+}-long TM6 (EMDB-41481) (PDB 8TPQ)	A444P Ca^{2+}-short TM6 (EMDB-41482) (PDB 8TPR)	A444P Ca^{2+}-bent TM6 (EMDB-41483) (PDB 8TPS)	A444P Ca^{2+}-long TM6/short TM6 (EMDB-41484) (PDB 8TPT)
Data collection and processing					
Magnification	×130,000	×105,000	×105,000	×105,000	×105,000
Voltage (kV)	200	300	300	300	300
Electron exposure (e–/Å^2)	30.0	59.2	59.2	59.2	59.2
Defocus range (μm)	-1.0 to -2.0	-0.9 to -1.9	-0.9 to -1.9	-0.9 to -1.9	-0.9 to -1.9
Pixel size (Å)	0.91	0.825	0.825	0.825	0.825
Symmetry imposed	C2	C2	C2	C2	C1
Micrographs	6,368	11,976	11,976	11,976	11,976
Initial particle images (no.)	1,322,332	4,885,672	4,885,672	4,885,672	4,885,672
Final particle images (no.)	51,093	5,199	174,312	17,404	84,643
Map resolution (Å)	3.64	3.35	2.85	2.97	3.01
FSC threshold	0.143	0.143	0.143	0.143	0.143
Map resolution range (Å)	3.6-4.4	3.5-4.3	2.9-3.7	3.1-3.9	3.1-3.9
Refinement					
Initial model used (PDB code)	6QMB	6QMB	6QMB	6QMB	6QMB
Model resolution (Å)	3.68	3.11	2.90	2.95	3.06
FSC threshold	0.5	0.5	0.5	0.5	0.5
Model resolution range (Å)	3.68-4.40	3.11-4.30	2.90-3.70	2.95-3.90	3.06-3.90
Map sharpening *B* factor (Å^2)	-111.6	-58.5	-89.3	-58.7	-71.8
Model composition					
Non-hydrogen atoms	9,118	9,052	9,456	9,170	8,908
Protein residues	1,168	1,154	1,184	1,176	1,150
Ligands	4	8	8	6	8
B factors (Å^2)					
Protein	54.0	86.2	84.7	108.4	96.1
Ligand	40.2	85.2	93.0	117.1	100.5
R.m.s. deviations					
Bond lengths (Å)	0.003	0.003	0.004	0.004	0.003
Bond angles (°)	0.526	0.612	0.567	0.995	0.616
Validation					
MolProbity score	1.38	1.81	1.79	1.81	1.61
Clashscore	5.34	9.69	11.57	10.21	7.81
Poor rotamers (%)	0	0.56	0.52	0	0
Ramachandran plot					
Favored (%)	97.53	95.69	96.70	95.96	96.94
Allowed (%)	2.47	4.31	3.30	4.04	3.06
Disallowed (%)	0	0	0	0	0

Extended Data

Structural basis of closed groove scrambling by a TMEM16 protein

Zhang Feng[1], Omar E. Alvarenga[2], Alessio Accardi[1,3,4#]

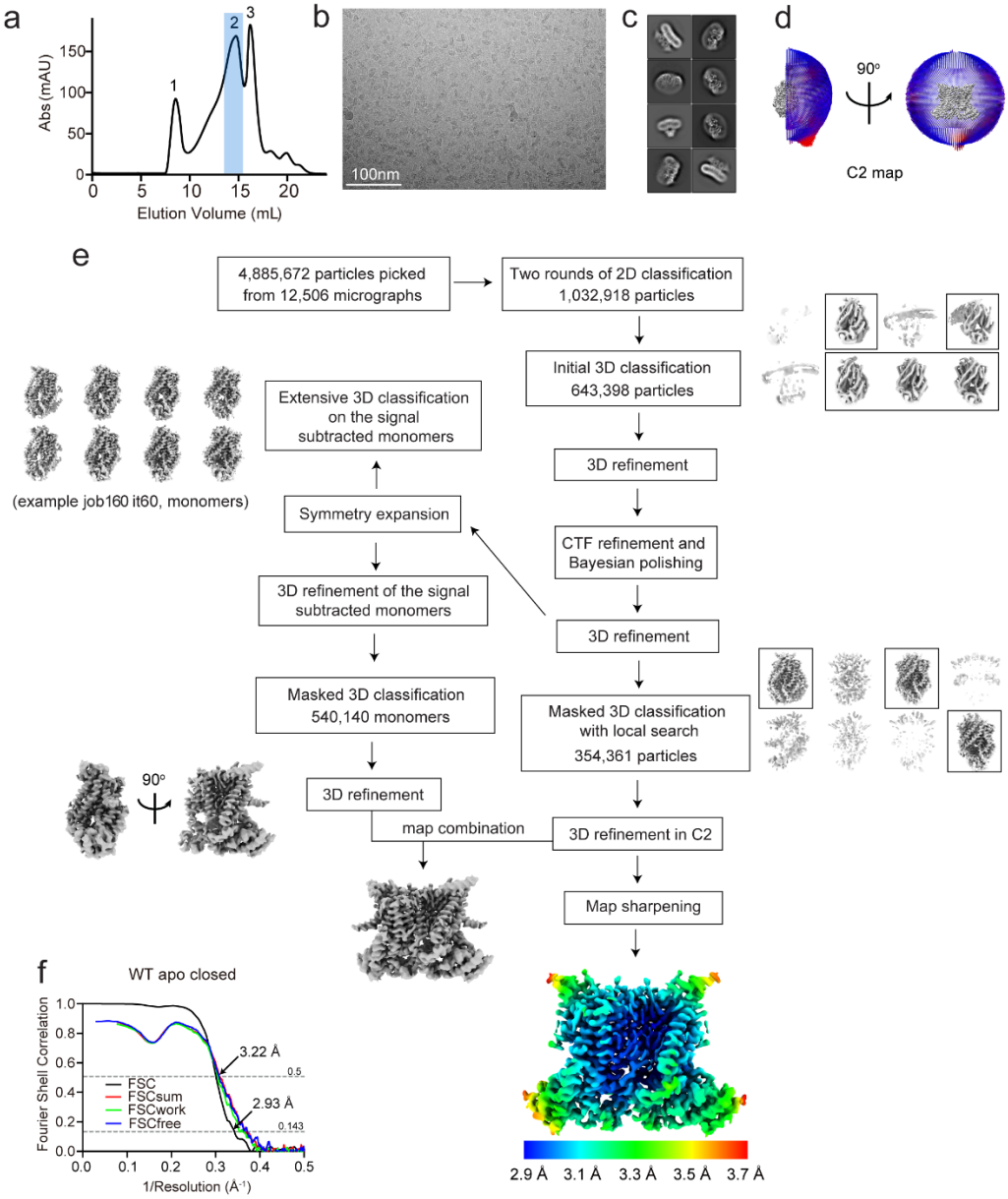

Extended Data Figure 1: **Structure determination of nhTMEM16 in the MSP1E3 nanodisc in 0 Ca^{2+}.** **a**, Size exclusion profile of the reconstituted nhTMEM16-nanodisc sample in 0 Ca^{2+}. The peak in the blue shadow contains the nhTMEM16-nanodisc complex. **b**, Representative micrograph. **c**, Representative 2D classes of the nhTMEM16-nanodisc complex. **d**, Angular distribution of the final reconstruction with C2 symmetry. **e**, Image processing workflow including symmetry expansion and 3D classifications of the signal subtracted monomers. Final masked reconstruction colored by local resolution calculated using the Relion implementation. **f**, FSC plots for nhTMEM16-nanodisc complex in 0 Ca^{2+}. FSC (black) is between the two half maps to determine the resolution of the reconstruction evaluated at 0.143 cutoff. FSCsum (red), FSCwork (green), and FSCfree (blue) are model validations evaluated at 0.5 cutoff.

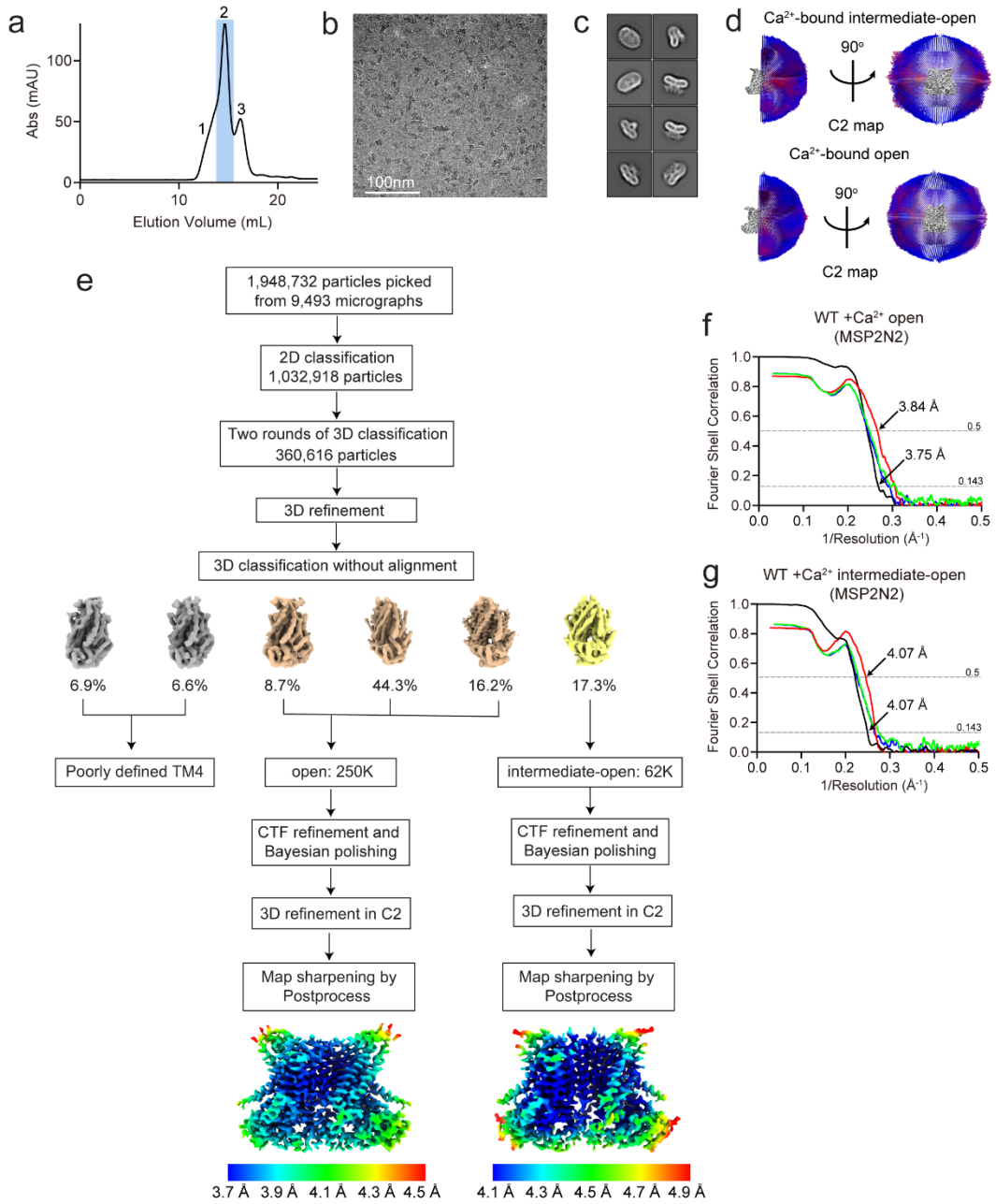

Extended Data Figure 2: **Structure determination of nhTMEM16 in the MSP2N2 nanodisc in the presence of Ca^{2+}**. **a**, Size exclusion profile of the reconstituted nhTMEM16-nanodisc sample in the presence of 0.5mM Ca^{2+}. The peak in the blue shadow contains the nhTMEM16-nanodisc complex. **b**, Representative micrograph. **c**, Representative 2D classes of the nhTMEM16-nanodisc complex. **d**, Angular distribution of the final reconstruction of the Ca^{2+}-bound intermediate-open (top) and Ca^{2+}-bound open (bottom) state. **e**, Image processing workflow. Final masked reconstruction colored by local resolution calculated using the Relion implementation. **f**, **g**, FSC plots for nhTMEM16-nanodisc complex in + Ca^{2+} in the MSP2N2 nanodisc. FSC (black) is between the two half maps to determine the resolution of the reconstruction evaluated at 0.143 cutoff. FSCsum (red), FSCwork (green), and FSCfree (blue) are model validations evaluated at 0.5 cutoff.

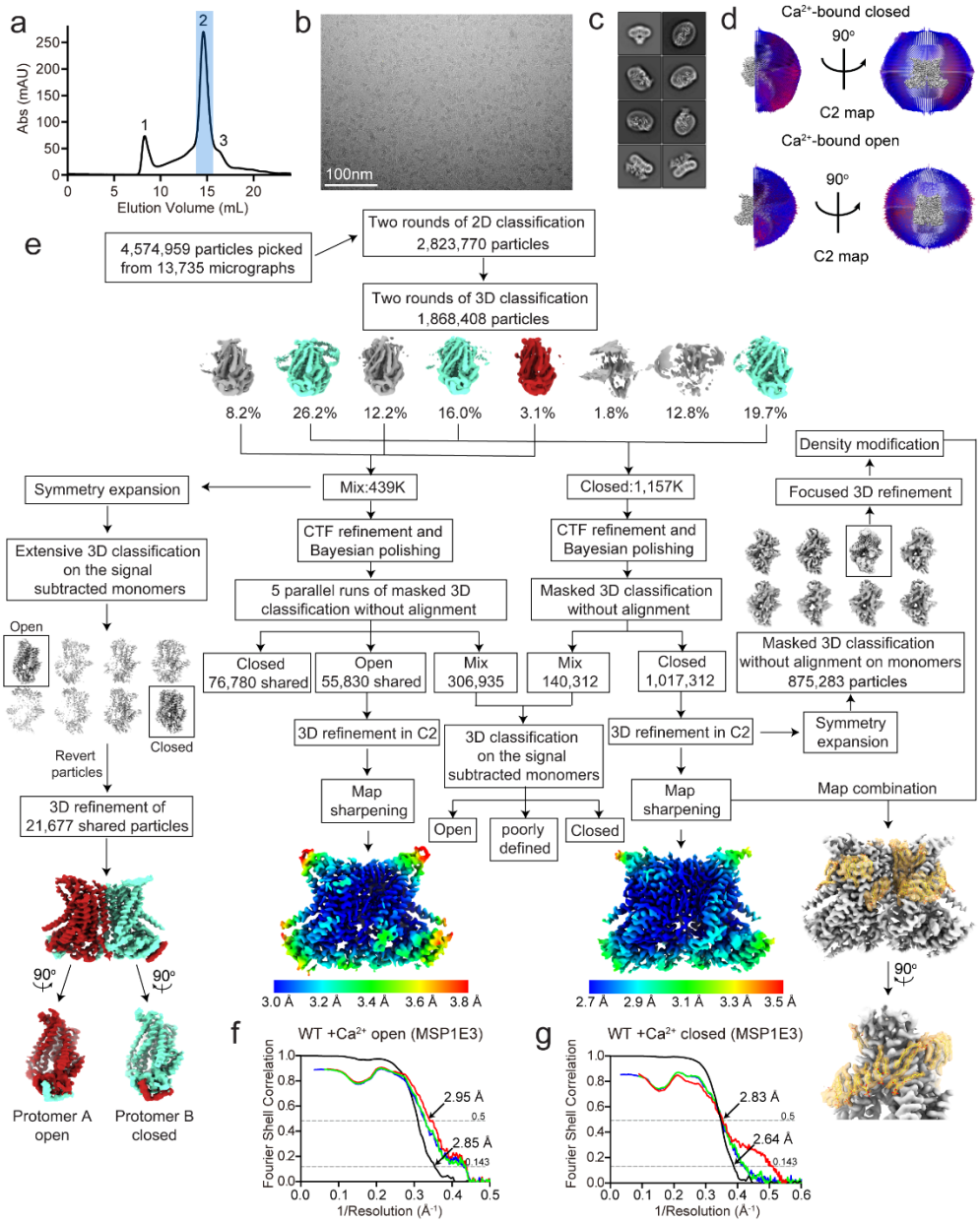

Extended Data Figure 3: **Structure determination of nhTMEM16 in the MSP1E3 nanodisc in the presence of Ca^{2+}**. **a**, Size exclusion profile of the reconstituted nhTMEM16-nanodisc sample in the presence of 0.5mM Ca^{2+}. The peak in the blue shadow contains the nhTMEM16-nanodisc complex. **b**, Representative micrograph. **c**, Representative 2D classes of the nhTMEM16-nanodisc complex. **d**, Angular distribution of the final reconstruction of the Ca^{2+}-bound closed (top) and Ca^{2+}-bound open (bottom) state. **e**, Image processing workflow including symmetry expansion and 3D classifications to identify monomers with well-resolved density for lipids to assist model building, and the open/closed dimers with one open and one closed groove. Final masked reconstruction colored by local resolution calculated using the Relion implementation. **f**, **g**, FSC plots for nhTMEM16-nanodisc complex in + Ca^{2+} in the MSP1E3 nanodisc. FSC (black) is between the two half maps to determine the resolution of the reconstruction evaluated at 0.143 cutoff. FSCsum (red), FSCwork (green), and FSCfree (blue) are model validations evaluated at 0.5 cutoff.

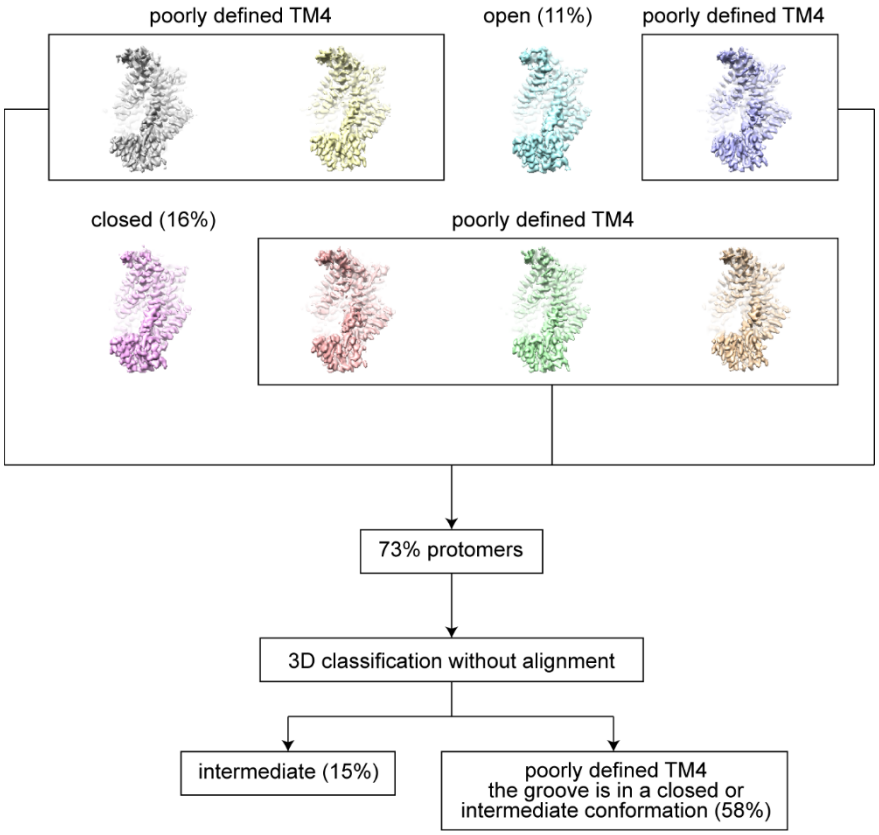

Extended Data Figure 4: **Classification of the symmetry-expanded protomers of WT nhTMEM16 in MSP1E3 nanodiscs from the particles of which the density around the groove region was not well resolved.**

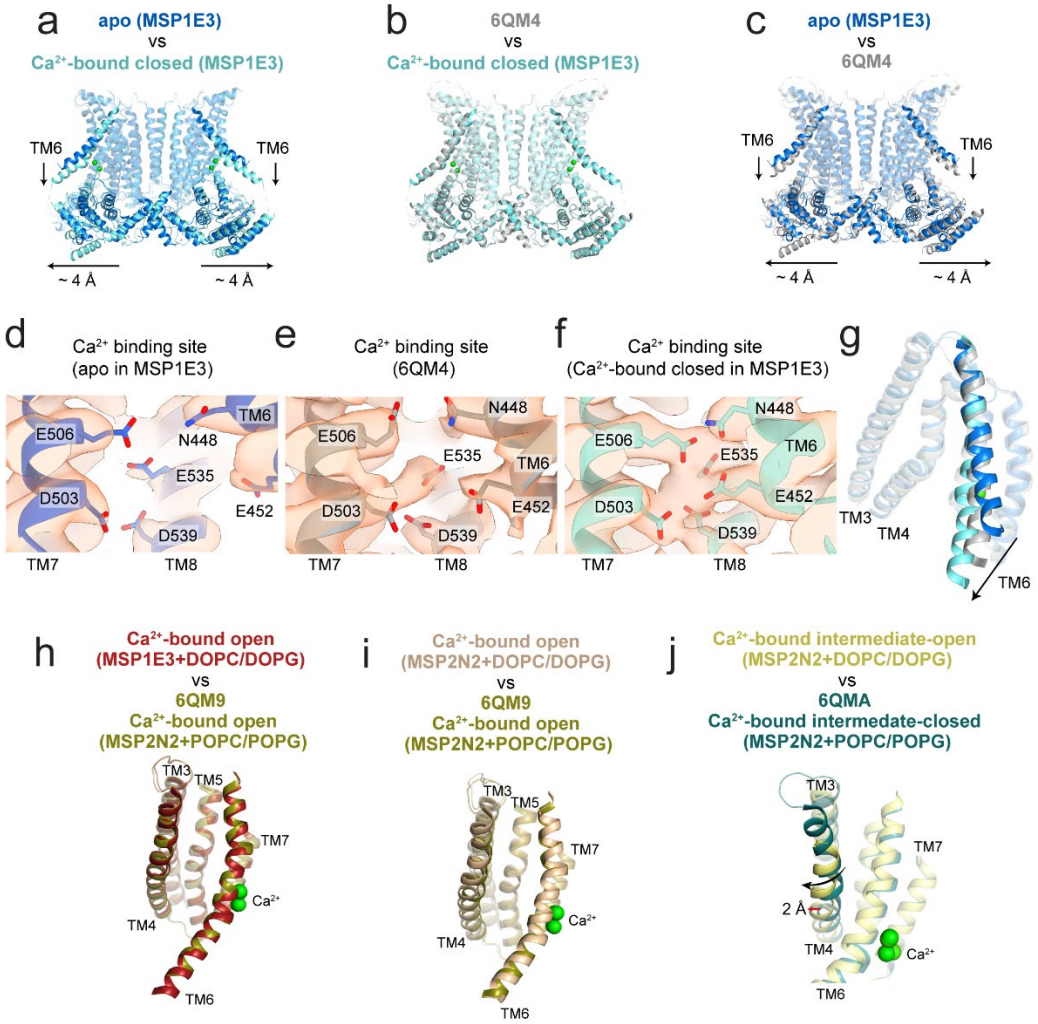

Extended Data Figure 5: **Structural characterization of the nhTMEM16 structures**. **a-c**, Structural alignment of nhTMEM16 structures determined in DOPC/DOPG lipids and MSP1E3 nanodiscs in apo (blue) and Ca^{2+}-bound closed state (cyan) to the previously reported putative apo 6QM4 conformation (gray). nhTMEM16 is viewed from the plane of the membrane from the side. Horizontal arrows at the bottom denote the ~4 Å displacement of the cytosolic domains away from the symmetry axis between the apo state and 6QM4. Vertical arrows denote the partial straightening of TM6 from the apo state to 6QM4. Superpositions of structures in panels **a-c** yield a Cα r.m.s.d of 1.23 Å (**a**), 0.67 Å (**b**), and 1.76 Å (**c**), respectively. **d-e**, Views of the Ca^{2+}-binding site in the Ca^{2+}-free state of nhTMEM16 from this study (**d**) (blue), the previously reported putative apo structure (PDBID: 6QM4, gray) (**e**) and the Ca^{2+}-bound closed state from this study (**f**). The density maps (contoured at 4.5 σ) are shown in orange. Weak residual density at the center of the Ca^{2+}-binding site is observed in 6QM4 (**e**). **g**, Structural alignment of the nhTMEM16 groove region of the structures in apo and Ca^{2+}-bound closed state from this study and 6QM4. An intermediate state of TM6 is observed in 6QM4. **h**, **i**, Comparison of the groove in the open state obtained in DOPC/DOPG lipids in MSP1E3 (**h**) or MSP2N2 (**i**) to the previously reported open structure determined in POPC/POPG lipids and MSP2N2 (PDBID: 6QM9) (olive). **j**, Comparison of the groove in the intermediate-open state in MSP2N2 (yellow) to the previously reported intermediate-closed structure (PDBID: 6QMA) (dark green).

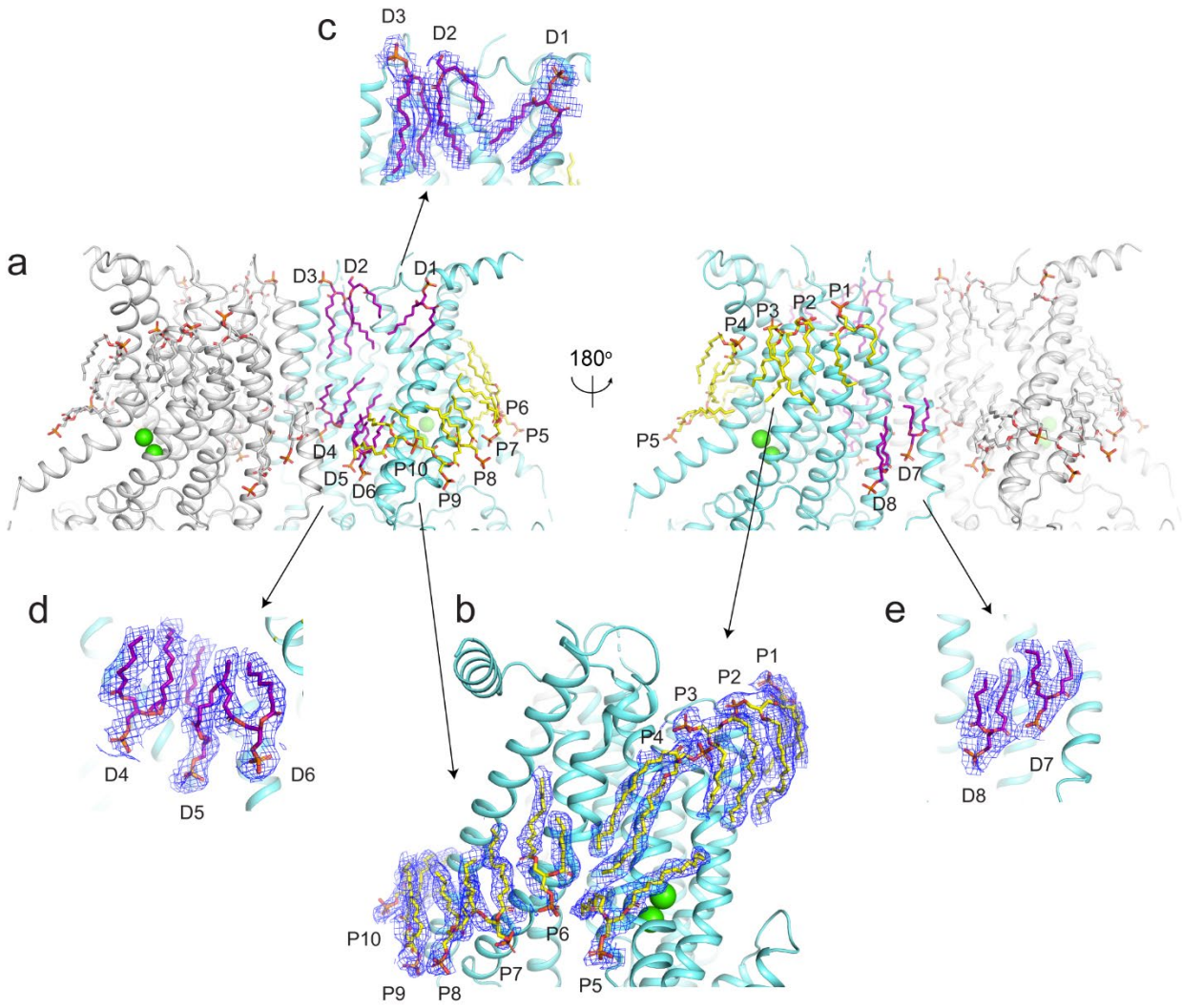

Extended Data Figure 6: **Lipid densities associated with nhTMEM16 in the Ca^{2+}-bound closed state**. **a**, Structure model of nhTMEM16 in the Ca^{2+}-bound closed state. Protomers in the dimer are colored in gray and cyan. Acyl chains of the built lipids are colored in yellow (at the closed groove) or magenta (at the dimer cavity) in one protomer and in gray in the other one. **b-d**, Close-up views of lipids at the closed groove (**b**) and the dimer cavity (**c** and **d**). Lipids are shown with mesh from the sharpened map in blue with σ=2.0. Respective lipids are labelled and Ca^{2+} ions are displayed as green spheres.

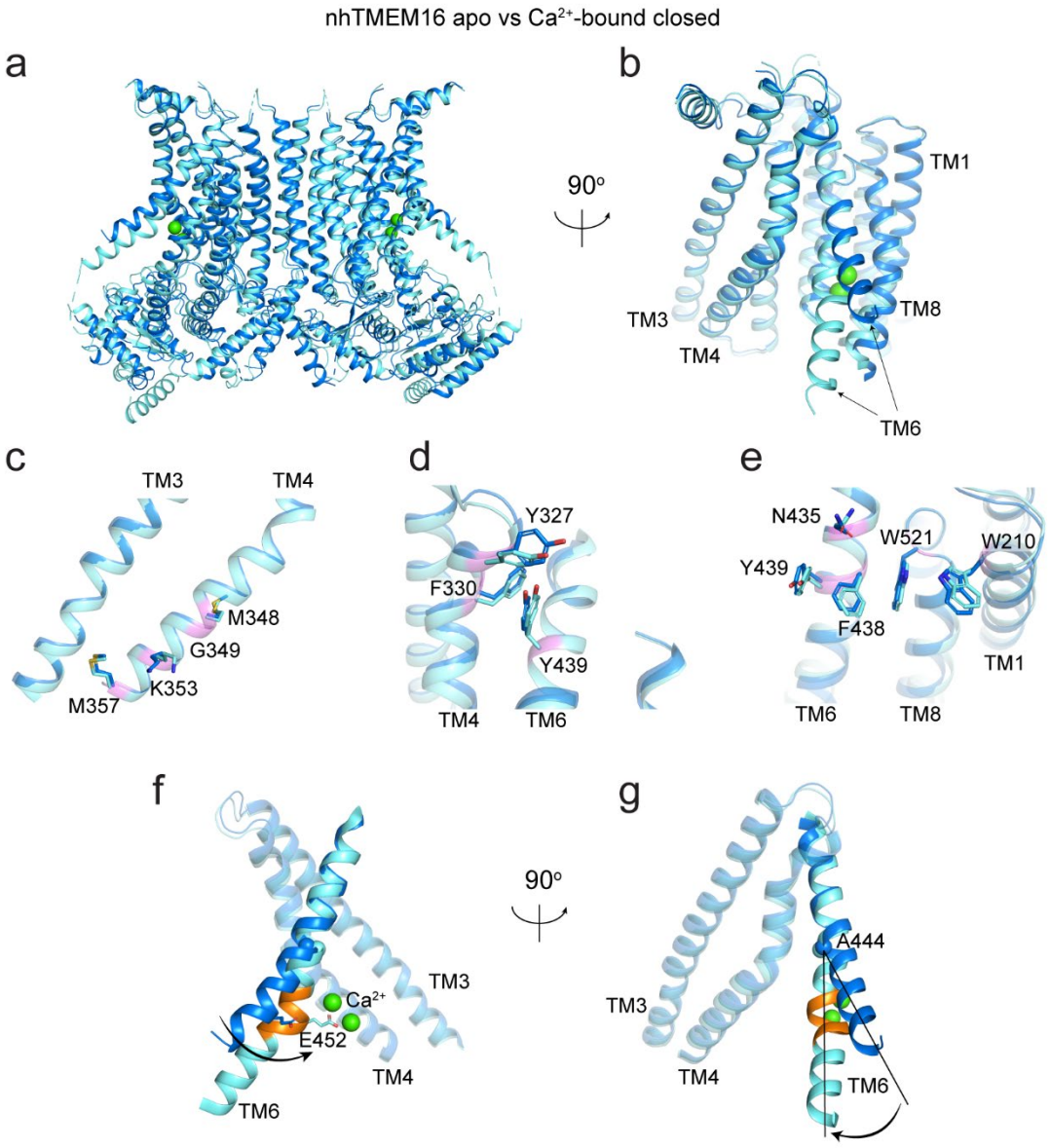

Extended Data Figure 7: **Structural comparison of nhTMEM16 apo with the Ca^{2+}-bound closed state**. **a**, Alignment of the apo (blue) with the Ca^{2+}-bound closed nhTMEM16 (cyan). **b**, Close-up view of the groove. Ca^{2+} ions are displayed as green spheres. **d-e**, Close-up views of the alignment of the residues coordinating lipids outside the groove in the Ca^{2+}-bound state with the equivalent residues in the apo state. Side chains are shown as sticks. Representative transmembrane helices are labelled. **f**, **g**, Conformational arrangements on the TM6 when transits from apo state (blue) to the Ca^{2+}-bound closed state (cyan). π-helical turn is colored in orange.

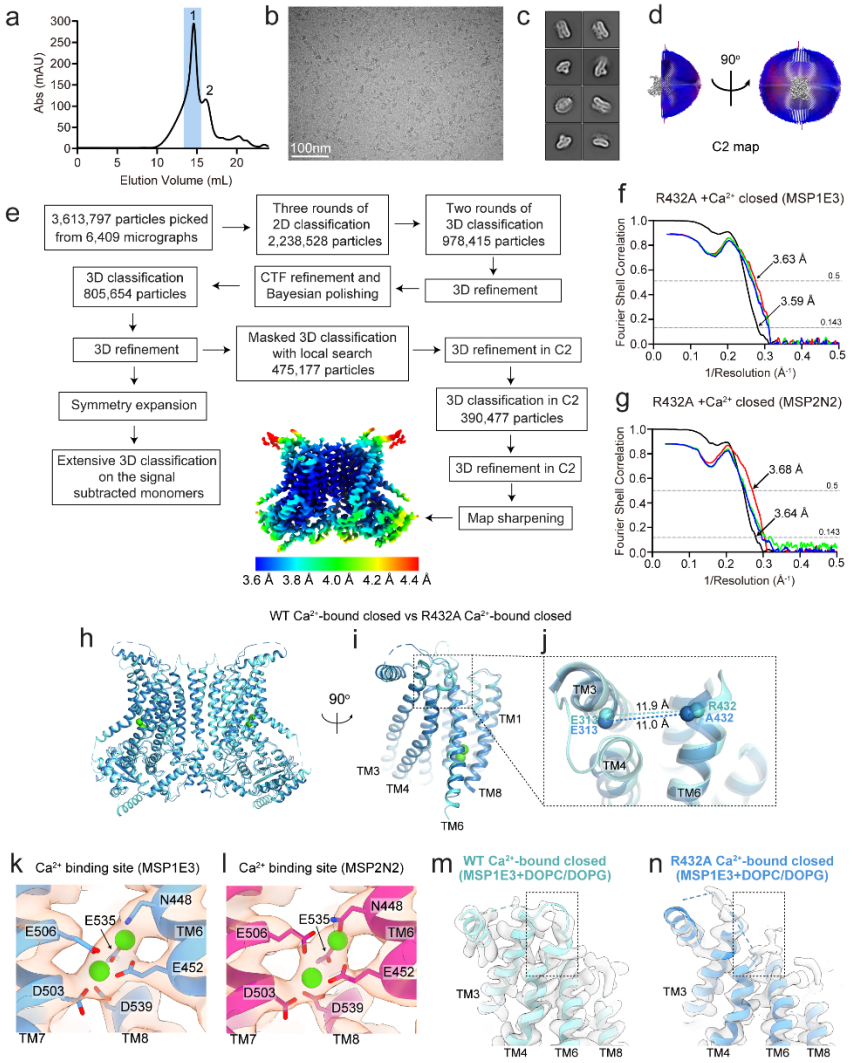

Extended Data Figure 8: **Structure determination and characterization of R432A nhTMEM16 in the MSP1E3 or MSP2N2 nanodisc in the presence of Ca^{2+}**. **a**, Size exclusion profile of the reconstituted the R432A nhTMEM16-nanodisc sample in the presence of 0.5mM Ca^{2+}. The peak in the blue shadow contains the R432A nhTMEM16-nanodisc complex. **b**, Representative micrograph. **c**, Representative 2D classes of the R432A nhTMEM16-nanodisc complex. **d**, Angular distribution of the final reconstruction in C2. **e**, Image processing workflow including symmetry expansion and 3D classifications to identify potential alternate conformations. Final masked reconstruction colored by local resolution calculated using the Relion implementation. **f**, **g**, FSC plots for R432A nhTMEM16-nanodisc complex in + Ca^{2+} in the MSP1E3 nanodisc (**f**) or MSP2N2 nanodisc (**g**). FSC (black) is between the two half maps to determine the resolution of the reconstruction evaluated at 0.143 cutoff. FSCsum (red), FSCwork (green), and FSCfree (blue) are model validations evaluated at 0.5 cutoff. **h-j**, Structural comparison of R432A nhTMEM16 in the MSP1E3 nanodisc (light blue) to WT nhTMEM16 in the Ca^{2+}-bound closed state (cyan) from the side (**h**) or front view (**i**). Colored spheres correspond to the position of the Cα atoms of E313 on TM3 and R432 (or A432) on TM6 and their distance is indicated (**j**). Ca^{2+} ions are shown as green spheres. **k**, **i**, Views of the Ca^{2+}-binding site in the R432A nhTMEM16 in + Ca^{2+} in the MSP1E3 nanodisc (**k**) or MSP2N2 nanodisc (**i**). **m**, **n**, Views of the upper groove region of nhTMEM16 in the Ca^{2+}-bound closed state (**m**) and R432A nhTMEM16 in the Ca^{2+}-bound closed state (**n**).

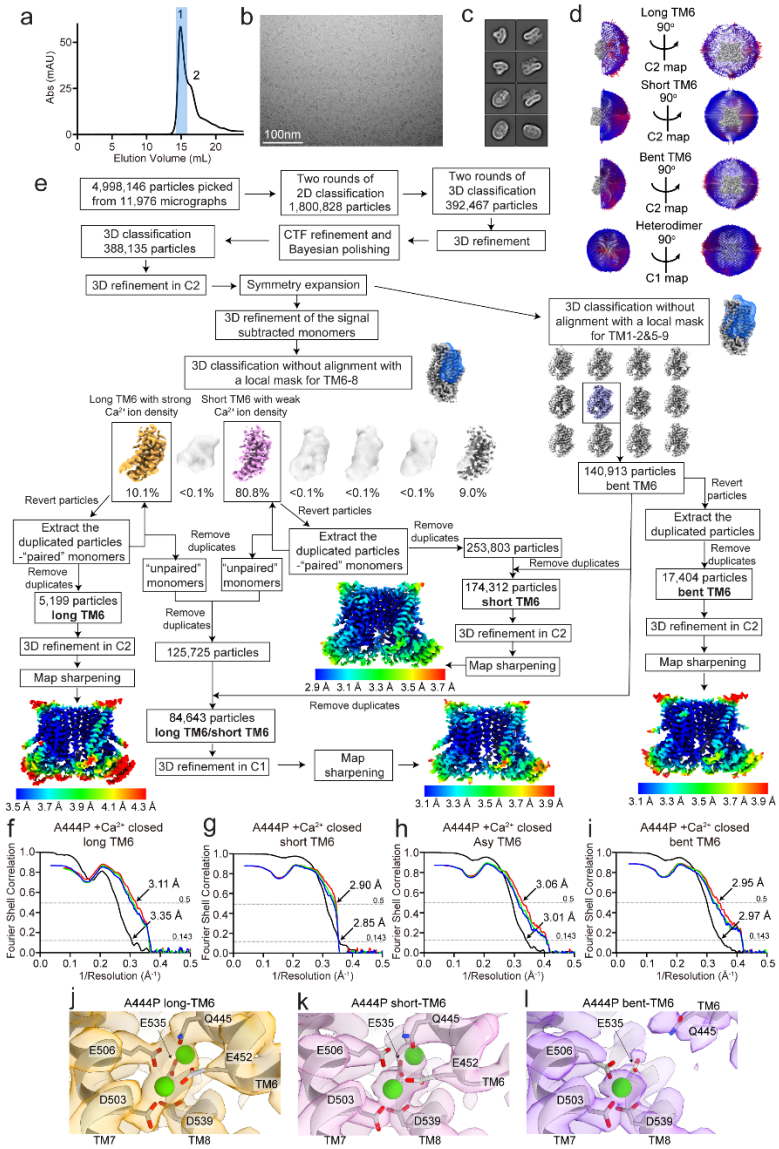

Extended Data Figure 9: **Structure determination of A444P nhTMEM16 in the MSP1E3 nanodisc in the presence of Ca^{2+}**. **a**, Size exclusion profile of the reconstituted the A444P nhTMEM16-nanodisc sample in the presence of 0.5mM Ca^{2+}. The peak in the blue shadow contains the A444P nhTMEM16-nanodisc complex. **b**, Representative micrograph. **c**, Representative 2D classes of the A444P nhTMEM16-nanodisc complex. **d**, Angular distribution of the final reconstruction in C2. **e**, Image processing workflow including symmetry expansion and classification to identify the four different conformations, the long TM6, short TM6, bent TM6 and long TM6/short TM6 A444P. Final masked reconstruction colored by local resolution calculated using the Relion implementation. **f-i**, FSC plots for A444P nhTMEM16-nanodisc complex in the MSP1E3 nanodisc in the Ca^{2+}-bound closed state with long TM6 (**f**), short TM6 (**g**), bent TM6 (**h**) and long TM6/ short TM6 (**i**). FSC (black) is between the two half maps to determine the resolution of the reconstruction evaluated at 0.143 cutoff. FSCsum (red), FSCwork (green), and FSCfree (blue) are model validations evaluated at 0.5 cutoff. **j-l**, Views of the Ca^{2+}-binding site of the nhTMEM16 mutant A444P in the long TM6 state (**j**), the short TM6 state (**k**) and the bent TM6 state (**l**) with map density colored in orange, pink and purple, respectively. Side chains of the Ca^{2+} coordinating residues are shown as sticks and the Ca^{2+} ions are displayed as green spheres.

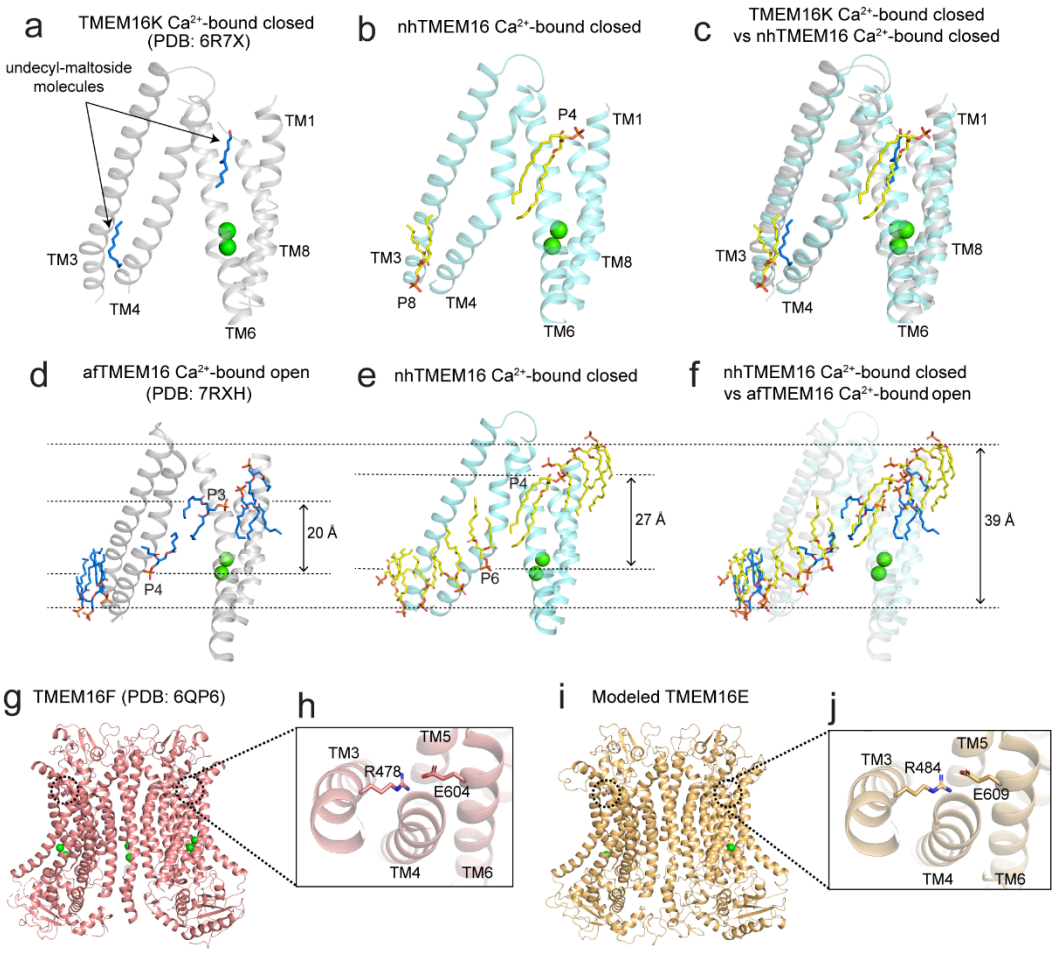

Extended Data Figure 10: **Comparison of the membrane thickness at open and closed groove and the conserved lipid/detergent binding sites and the salt bridge in mammalian TMEM16s**. **a**, Two undecyl-maltoside molecules (shown in blue) were resolved in the cryo-EM structure (PDB: 6R7X, shown in gray) of TMEM16K in the Ca^{2+}-bound closed state. **b**, The resolved lipids P4 and P8 associated with the closed groove of nhTMEM16. **c**, Alignment of the closed state of nhTMEM16 with TMEM16K. Ca^{2+} ions are displayed as green spheres. **d**, Lipids (shown in blue) outside of the open groove of afTMEM16 (PBD:7RXH, shown in gray). The distance between the phosphate atoms of the heads of P3 and P4 in the outer leaflet and inner leaflet is ~20 Å. **e**, Lipids (shown in yellow) outside of the closed groove of nhTMEM16 (shown in cyan). The distance between the phosphate atoms of the heads of P4 and P6 in the outer leaflet and inner leaflet is ~27 Å. **f**, Alignment of the rearrangements of the lipids outside of the open with the closed groove. The ~39 Å membrane thickness is defined by the distance between the phosphate atoms of the heads of lipids away from the groove region and perpendicular to the membrane. Ca^{2+} ions are displayed as green spheres. **g, i**, The cryo-EM structure of TMEM16F (PDB:6QP6) in the Ca^{2+}-bound closed state (**g**) and the predicted model of TMEM16E (**i**) by SWISS-MODEL (Waterhouse, Bertoni et al. 2018) based on TMEM16F (PDB:6QP6). The conserved salt bridge in the two structures is denoted by a dashed circle. **h**, **j**, Closed-up views of the salt bridge of R478-E604 in TMEM16F (**h**) and R484-E609 in TMEM16E (**i**).

References

Waterhouse, A., M. Bertoni, S. Bienert, G. Studer, G. Tauriello, R. Gumienny, F. T. Heer, T. A. P. de Beer, C. Rempfer, L. Bordoli, R. Lepore and T. Schwede (2018). "SWISS-MODEL: homology modelling of protein structures and complexes." Nucleic Acids Res **46**(W1): W296-w303.

Supplementary Table 1: Residue ranges and side chain truncations

	WT apo	WT Ca^{2+}-closed MSP1E3	WT Ca^{2+}-open MSP1E3	WT Ca^{2+}-intermediate MSP2N2	WT Ca^{2+}-open MSP2N2	R432A Ca^{2+}-closed MSP1E3
Included Residues	15-100, 109-413, 426-457, 477-585, 597-651, 689-718	15-413,426-467, 477-585, 595–642, 666-685, 688–718	15-470, 477-586, 595-650, 667-670, 686-719	16-94, 102-266, 276-317, 330-397, 401-411, 428-465, 479-584, 598-628, 702-712	16-251, 253-417, 421-466, 479-584, 596-646, 690-715	16-319, 330-415, 425-462, 478-585, 598-626, 630-648, 689-716
Side chain truncations	E15, E60, N61, N138, K140, Y218, K325, Q412, F426, V454, V455, Y457, E477, E496, F567, S629, L651, T689, E692, M693, M701, M711, E713	E15, N61, D74, Y81, H98, K140, Q412, F463, K465, E477, E496, F567, S629, R639, K669, E676, E677, T689, E692, R710, E713	E15, E32, E35, H58, E129, K140, E260, E266, Q326, Y327, K353, F416, E418, K419, E425, K467, Q468, L469, K470, E477, E481, E496, E638, E649, N650, E668, K669, R672, E673, L675, E677, R680, Q681, R685, H687, R699, E706, R710	E35, N61, D107, E129, K140, K142, K157, E158, Q255, E264, H265, E266, K283, F330, L331, T342, F403, F406, R408, T410, Y439, F463, Q464, K465, H479, E480, R490, E496, K598, D628, E703, E706, R709, R710, I712	E32, E35, K140, Q256, E260, E266, E274, Q326, Y327, K353, Q412, T413, L414, F416, S417, L421, E425, K459, F463, Q464, K465, E481, E496, K598, R636, E638, R645, E692, R699, E703, E706, R709, R710, E713	K27, E32, E35, E55, E60, K78, R82, D87, V94, D100, Q106, D107, E108, N138, K142, E313, E318, I399, F403, F406, R408, Q412, T415, E425, F426, Q460, E478, E480, E481, E484, K598, E635, R636, K637, E638, R639, K643, R645, Q648, E692, R709, R710, M711, E713, L716
	R432A Ca^{2+}-closed MSP2N2	A444P Ca^{2+}-long TM6	A444P Ca^{2+}-short TM6	A444P Ca^{2+}-bent TM6	A444P Ca^{2+}-long TM6/short TM6	
Included Residues	16-95, 102-268, 274-319, 331-408, 426-465, 481-585, 598-642, 694-717	16-93, 111-267, 277-323, 326-408, 428-463, 481-585, 599-627, 630-645, 689-715	16-97, 102-106, 108-320, 324-409, 428–455, 481-585, 598–643, 689–715	16-70, 72-106, 108-267, 277-323, 326-408, 428-455, 481-585, 599-647, 690-715	Chain A: 16-93, 111-267, 277-323, 326-408, 428-463, 481-585, 599-627, 630-647, 689-715	Chain B: 16-93, 111-267, 277-323, 326-408, 428-454, 481-585, 599-627, 630-647, 689-715
Side chain truncations	E32, N61, D74, L75, K78, Y81, S95, Q106, E108, K140, Q215, E264, E268, E274, K277, E313, I316, E318, F335, L404,	S16, K27, E32, D34, R45, H58, E60, N61, E62, D74, K78, Q79, Y81, R82, L85, D87, N128, E129, T137, N138,	N61, D74, K78, Y81, Q103, D107, N138, K140, E268, E274, Y320, K325, Q326, H401, F403, L404, N405, R408, E481, K598,	S16, D34, Q42, E60, N61, D74, K78, Y81, R82, L85, D87, H98, I101, Q106, E108, N128, E129, T137, N138, K140, K142, K237, Q255, E262,	S16, K27, E32, D34, R45, H58, E60, N61, E62, D74, K78, Q79, Y81, R82, L85, D87, N128, E129, T137, N138,	S16, K27, E32, D34, R45, H58, E60, N61, E62, D74, K78, Q79, Y81, R82, L85, D87, N128, E129, T137, N138,

	F406, W407, F426, Q427, Y457, Q460, F463, Q464, K465, E496, S629, K634, R636, R639, T642, W695, Q696, R699, E703, E706, E713	K140, K237, Q255, E262, E264, K277, N317, E318, Y320, Q326, L328, D364, L400, R408, F463, E482, Q487, L632, Q633, K634, E635, R636, E638, R639, Q641, T642, K643, R645, M693, R699, E703, R710, E713, Q715	D628, L632, K634, E635, E638, R639, K643, T689, R699, Q714	E264, K277, N317, E318, V319, Y320, Q326, L328, D364, F403, R408, F449, T451, E452, V453, V454, V455, E482, E484, E491, D628, L632, K634, E635, K637, E638, R639, Q641, T642, K643, K644, R645, L646, L647, E691, E692, M693, E706, R709, R710, E713	K140, W141, K142, K237, Q255, E262, E264, H265, E266, K277, N317, E318, Y320, Q326, L328, D364, L400, R408, K459, Q461, F463, E482, E484, Q487, E491, L627, P630, L632, Q633, K634, E635, R636, E638, R639, Q641, T642, K643, R645, L646, M693, R699, Q702, E703, E706, R709, R710, E713, Q715	K140, W141, K142, K237, Q255, E262, E264, H265, E266, K277, N317, E318, Y320, Q326, L328, D364, L400, R408, E482, E484, Q487, E491, L627, P630, L632, Q633, K634, E635, R636, E638, R639, Q641, T642, K643, R645, L646, M693, R699, Q702, E703, E706, R709, R710, E713, Q715